

PNE-1110

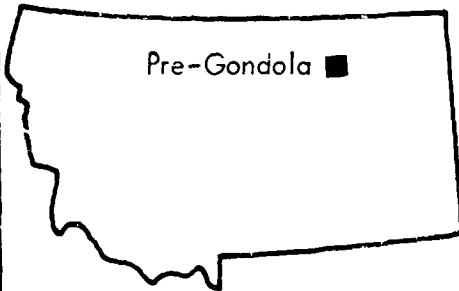


Plowshare

civil, industrial and scientific uses for nuclear explosives

UNITED STATES ARMY CORPS OF ENGINEERS

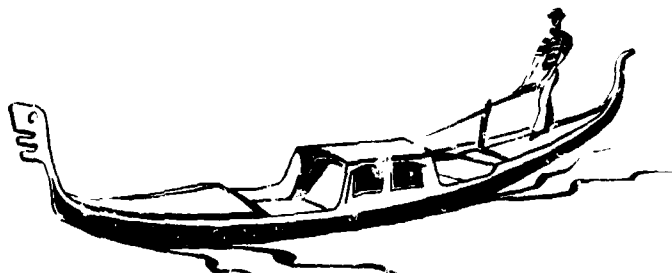
FORT PECK RESERVOIR  
MONTANA



Pre-Gondola ■

PROJECT

**PRE-GONDOLA I**



DISTRIBUTION STATEMENT A

Approved for public release;  
Distribution Unlimited

LIDAR OBSERVATIONS OF THE PRE-GONDOLA I CLOUDS

JOHN W. DELANAS

RONALD T. H. COLLIS

Stanford Research Institute  
Menlo Park, California

Reproduced by  
NATIONAL TECHNICAL  
INFORMATION SERVICE  
Springfield, Va. 22151

D D C

JAN 25 1972

U. S. Army Engineer Nuclear Cratering Group  
Livermore, California

Issued: July 1967

82

AD735639

PNE-1110

Final Report

LIDAR OBSERVATIONS OF THE PRE-GONDOLA I CLOUDS

Prepared for:

The U. S. Atomic Energy Commission  
University of California  
Lawrence Radiation Laboratory  
P. O. Box 808  
Livermore, California 94551

Contract AT (04-3)-115  
Project Agreement Number 66

John W. Oblanas  
Ronald T. H. Collis  
Stanford Research Institute  
Menlo Park, California  
SRI Project 6268

January 1967

# LEGAL NOTICE

This report was prepared as an account of Government sponsored work. Neither the United States, nor the Commission, nor any person acting on behalf of the Commission

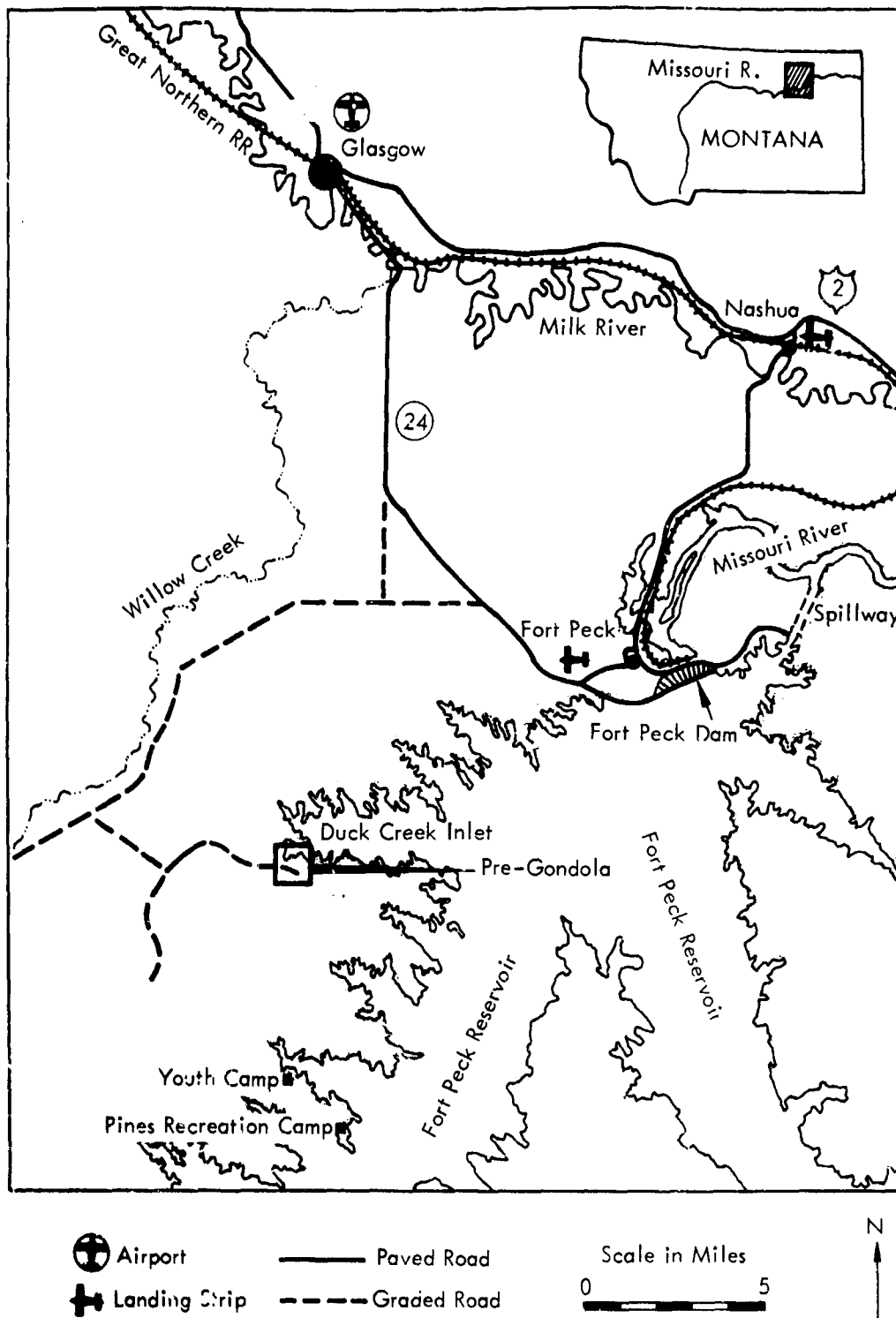
A. Makes any warranty or representation, expressed or implied, with respect to the accuracy, completeness, or usefulness of the information contained in this report, or that the use of any information apparatus, method, or process disclosed in this report may not infringe privately owned rights; or

B. Assumes any liabilities with respect to the use of, or for damages resulting from the use of any information, apparatus, method, or process disclosed in this report.

As used in the above, "person acting on behalf of the Commission" includes any employee or contractor of the Commission, or employee of such contractor, to the extent that such employee or contractor of the Commission, or employee of such contractor prepares, disseminates, or provides access to, any information pursuant to his employment or contract with the Commission, or his employment with such contractor.

ACCESSION TAG		
CFSTI	WRITE SECTION	<input checked="" type="checkbox"/>
DDC	DIFF. SECTION	<input type="checkbox"/>
UNCLASSIFIED		<input type="checkbox"/>
DISTRIBUTION AVAILABILITY CODES		
DIST.	AVAIL.	and/or SPECIAL
A		

Printed in USA. Available from the Clearinghouse for Federal Scientific and Technical Information, National Bureau of Standards, U. S. Department of Commerce, Springfield, Virginia 22151  
 Price: Printed Copy \$3.00; Microfiche ~~\$0.65~~ .75



PROJECT PRE-GONDOLA LOCATION MAP

## ABSTRACT

This report describes lidar (laser radar) observations of the dust and steam clouds that resulted from the PRO-CONDOLA I series of four chemical explosions made near Fort Peck Reservoir, Montana, during October-November 1966. The neodymium lidar was well able to track the clouds even when they became too tenuous to be seen visually or photographed.

Observational data were analyzed to obtain cloud dimension, height, volume, rate of growth, volume backscatter coefficient and relative density variations.

It is concluded that lidar tracking techniques can provide unique information on the position, motion, rate of growth, and internal structure of visible and sub-visible clouds resulting from large-scale explosions, and recommendations are made for improving the operational efficiency of the technique.

### ACKNOWLEDGEMENT

The SRI team who carried out this project in the field consisted of:

Dr. M. G. H. Ligda, Aerophysics Laboratory Manager

R. T. H. Collis, Head, Radar Aerophysics Group

J. W. Oblanas

G. E. Davis

A. H. Smith

In addition, J. E. Alder assisted with data reduction.

The SRI team wishes to express their appreciation for the helpful interest and assistance of Lt. Col. Maurice Kurtz, Messrs. Robert Rohrer, and Walter Day, and other personnel of the Pre-GONDOLA I Project, and Mr. Don Beckman, Fort Peck Area Engineer, and his staff of the U. S. Army Corps of Engineers.

## CONTENTS

ABSTRACT . . . . .	2
ACKNOWLEDGMENT . . . . .	3
LIST OF ILLUSTRATIONS . . . . .	6
LIST OF TABLES . . . . .	9
I INTRODUCTION . . . . .	10
II SUMMARY, CONCLUSIONS, AND RECOMMENDATIONS . . . . .	13
A. Program Summary . . . . .	13
B. Conclusions . . . . .	14
C. Recommendations . . . . .	15
1. General . . . . .	15
2. Observational Procedure . . . . .	16
3. Equipment . . . . .	16
a. System Detection Performance . . . . .	16
b. Pulse-Repetition Frequency . . . . .	17
c. Data Recording . . . . .	17
d. Data Display . . . . .	17
e. Lidar Pointing Angles . . . . .	18
f. Equipment Calibration . . . . .	18
4. Analysis Techniques . . . . .	18
III INSTRUMENTATION AND DATA FORMAT . . . . .	19
A. Mark V Lidar . . . . .	19
B. Electronics and Data Recording Equipment . . . . .	22
C. Data Format . . . . .	24

IV DETAILED DISCUSSION	27
A. Shot Bravo, 25 October 1966	27
1. Cloud Tracking	27
2. Data Analysis	29
B. Shot Charlie, 28 October 1966	29
1. Cloud Tracking	31
2. Data Analysis	31
C. Shot Alfa, 1 November 1966	44
1. Cloud Tracking	44
a. Visible Cloud	44
b. Sub-Visible Cloud	44
2. Further Analysis of the Data	46
D. Shot Delta, 4 November 1966	65
1. Cloud Tracking	65
2. Data Analysis	67
REFERENCES	72



## ILLUSTRATIONS

### FIGURES

1 Mark V Neodymium Lidar . . . . .	12
2a Mark V LIDAR Optical Diagram . . . . .	21
2b Block Diagram of the Mark V Lidar Electronics . . . . .	23
3 Typical Lidar Return Signal - Alfa . . . . .	25
4 Lidar-Beam Geometry . . . . .	26
5 Volume Estimate of the Visible Cloud - Bravo . . . . .	30
6 Horizontal Projection of the Visible Cloud Boundaries - Charlie; Time: 1:58 to 2:52 Min . . . . .	33
7 Horizontal Projection of the Visible Cloud Boundaries - Charlie; Time: 3:36 to 4:35 Min . . . . .	34
8 Horizontal Projection of the Visible Cloud Boundaries - Charlie; Time: 5:04 to 6:23 Min . . . . .	35
9 Horizontal Projection of the Visible Cloud Boundaries - Charlie; Time: 6:55 to 8:21 Min . . . . .	36
10 Horizontal Project of the Visible Cloud Boundaries - Charlie; Time: 9:21 to 10:37 Min . . . . .	37
11 Horizontal Projection of the Visible Cloud Boundaries - Charlie; Time: 11:15 to 13:07 Min . . . . .	38
12 Relative Density Variations of the Visible Cloud - Vertical Profile, Charlie . . . . .	39
13 Relative Density Variations of the Sub-Visible Cloud - Horizontal Profile - Charlie . . . . .	40
14 Volume Estimate of the Visible Cloud - Charlie . . . . .	41
15 Horizontal Cross Section of the Sub-Visible Cloud at 5°, 10°, 17°, and 25° Elevation Angles - Charlie . . . . .	42
16 Angular Relationships of the Lidar Shots of Figure 15 - Charlie . . . . .	43
17 Initial Rise of Cloud Top - Alfa . . . . .	44

18	Lateral Growth of the Visible Cloud - Alfa	45
19	Radial Depth of the Visible Cloud - Alfa	46
20	Lateral Growth of the Sub-Visible Cloud - Alfa	47
21	Radial Depth of the Sub-Visible Cloud - Alfa	48
22	Plan View - Rough Indication of Dispersal of the Three Cloud Phases - Alfa	49
23	Backscatter Coefficient of the Visible and Sub-Visible Clouds - Alfa	50
24	Horizontal Projection of the Visible Cloud - Alfa, Time: 1:42 to 2:18 Min	51
25	Horizontal Projection of the Visible Cloud - Alfa, Time: 2:49 to 3:27 Min	52
26	Horizontal Projection of the Visible Cloud - Alfa, Time: 3:47 to 4:17 Min	53
27	Horizontal Projection of the Visible Cloud - Alfa, Time: 4:44 to 5:22 Min	54
28	Horizontal Projection of the Visible Cloud - Alfa, Time: 5:43 to 6:22 Min	55
29	Horizontal Projection of the Visible Cloud - Alfa, Time: 6:59 to 7:41 Min	56
30	Horizontal Projection of the Visible Cloud - Alfa, Time: 8:20 to 9:17 Min	57
31	Horizontal Projection of the Visible Cloud - Alfa, Time: 9:46 to 10:27 Min	58
32	Horizontal Projection of the Visible Cloud - Alfa, Time: 10:54 to 11:41 Min	59
33	Horizontal Projection of the Visible Cloud - Alfa, Time: 12:10 to 13:31 Min	60
34	Horizontal Projection of the Visible Cloud - Alfa, Time: 14:07 to 16:20 Min	61
35	Horizontal Projection of the Visible Cloud - Alfa, Time: 17:01 to 18:00 Min	62

36	Horizontal Projection of the Visible Cloud - Alfa, Time: 18:24 to 18:58 Min . . . . .	63
37	Volume Estimate of Visible and Sub-Visible Cloud - Alfa . . . . .	64
38	Delta Event - Ground Track of Sub-Visible Cloud . . . . .	68
39	Approximate Density Contours - Sub-Visible Cloud Inferred from Relative Signal Amplitude Measurements - Delta; Time: 3:00 Min . . . . .	69
40	Approximate Density Contours - Sub-Visible Cloud Inferred from Relative Signal Amplitude Measurements - Delta; Time: 6:00 Min and 8:15 Min . . . . .	70
41	Approximate Density Contours - Sub-Visible Cloud Inferred from Relative Signal Amplitude Measurements - Delta; Time: 10:00 Min . . . . .	71

TABLES

TABLES									
I Data Summary	.	.	.	.	.	.	.	.	13
II Mark V Lidar Characteristics	.	.	.	.	.	.	.	.	20

## I INTRODUCTION

This Final Report presents the results obtained from the lidar (laser radar) observations of the Pre-GONDOLA I test series. Project Pre-GONDOLA I was a series of chemical explosive single-charge cratering experiments in weak, wet clay-shale conducted by the U. S. Army Engineer Nuclear Cratering Group (NCG) as a part of the joint Atomic Energy Commission - Corps of Engineers nuclear excavation research program. The purpose of the Pre-GONDOLA I Cratering Calibration Series was to calibrate the project site with respect to its cratering characteristics and to provide a basis for design of the proposed 140-ton Pre-GONDOLA II and the Pre-GONDOLA III row-charge cratering detonations in the same medium.

The Pre-GONDOLA I detonations occurred in Valley County, near the edge of the Fort Peck Reservoir approximately 18 miles south of Glasgow, Montana, as follows:

<u>Event</u>	<u>Date</u>	<u>Time (MST)</u>	<u>Longitude</u>	<u>Latitude</u>
Bravo	25 October 1966	1000:00.760	W 106°38'24.894"	N 47°55'46.154"
Charlie	28 October 1966	1200:00.654	W 106°38'29.974"	N 47°55'46.154"
Alfa	1 November 1966	1000:00.275	W 106°38'15.325"	N 47°55'46.570"
Delta	4 November 1966	1000:00.032	W 106°38'38.134"	N 47°55'48.077"

The four 20-ton (nominal) spherical charges of liquid explosive nitromethane ( $\text{CH}_3\text{NO}_2$ ) resulted in the following craters:

<u>Event</u>	<u>Tons</u>	<u>Depth of Burst</u>		<u>Apparent Crater Radius</u>		<u>Apparent Crater Depth</u>	
		<u>ft</u>	<u>m</u>	<u>ft</u>	<u>m</u>	<u>ft</u>	<u>m</u>
Charlie	19.62	42.49	12.95	80.4	24.50	32.6	9.94
Bravo	19.36	46.25	14.10	78.5	23.93	29.5	8.99
Alfa	20.35	52.71	16.07	76.1	23.19	32.1	9.78
Delta	20.24	56.87	17.34	65.1	19.84	25.2	7.68

The overall objectives of the lidar portion of the Pre-CONDOLA I Cloud Development Technical Program were to assess the capability of the lidar equipment to accomplish the following:

- (1) Observe the cloud during various stages of its life
- (2) Determine its volume or extent
- (3) Determine the distribution of matter within the cloud
- (4) Determine its rate of growth and velocity

Lidar is a ~~radar~~ apparatus operating in the optical rather than the microwave portion of the electromagnetic spectrum. Because of the great decrease in operating wavelength over that of the microwave radar, the lidar is capable of detecting energy backscattered from the visually clear atmosphere (and from discontinuities therein) as well as from natural and man-made clouds. The Mark V lidar (see Figure 1) consists of a pulsed laser source operating in the near infrared at a wavelength of  $1.06 \mu$ , an energy detector, the necessary beam-defining optics, and data display and recording equipment. Not shown in the figure are the magnetic disc recorder, the 35 mm recording camera and the sighting telescope used to aim the lidar. A detailed description of the lidar equipment used in the Pre-CONDOLA I observations is presented in Section II.

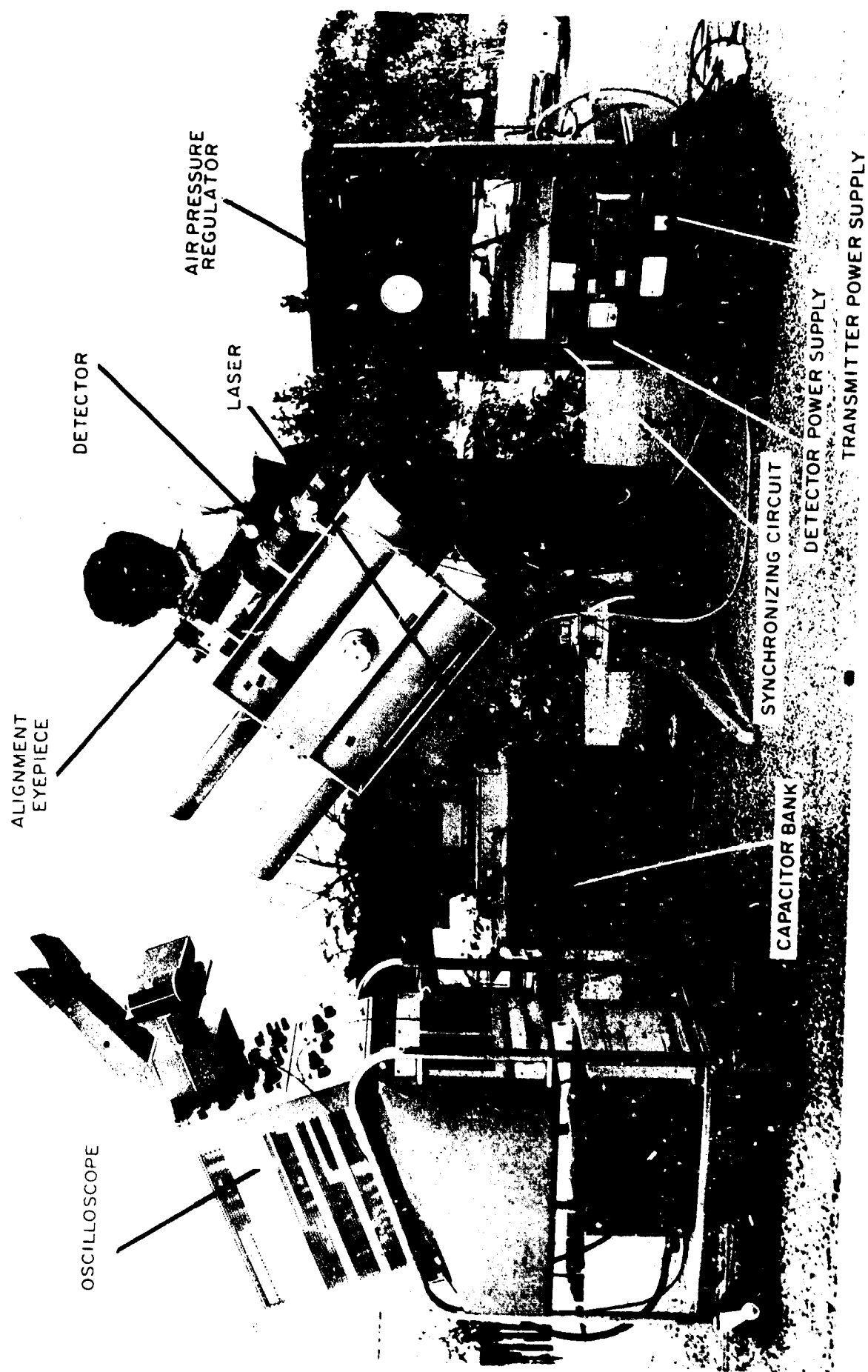


FIG. 1 MARK V NEODYMIUM LIDAR

## II SUMMARY, CONCLUSIONS, AND RECOMMENDATIONS

### A. Program Summary

The lidar equipment was assembled, aligned, and checked out at the site near Fort Peck, Montana on 21 October, in preparation for the first event on 25 October 1966. Lidar observations were taken of the visible cloud during the first event, and of the visible and sub-visible clouds during the remaining three events.

Table I summarizes the data obtained from the four events.

TABLE I DATA SUMMARY

Event	Number of Lidar Observations	Tracking Time (Minutes)	Maximum Detection Range		Observed Cloud Heights** (m)
			From GZ (m)	From Lidar (m)	
Bravo	50*	14*	2570	3630	932.2
Charlie	101	30	1900	3100	834.0
Alfa	87	22	2660	4010	775.6
Delta	117	15	5625	4125	—

\* Run terminated early because cloud drifted behind equipment shelter

\*\* All heights in this report are referenced to surface ground zero of the representative event. All ranges are referenced to the lidar location.

A peak firing rate of 6 pulses per minute was attained during the first three events; because of simplification of the data-recording format, a peak firing rate of 12 pulses per minute was achieved during the Delta event.

In addition, 34 lidar observations were made of the clear-air return in the vicinity of the lidar. These data were used in the calculation of volume backscatter coefficients.

The availability of four separate detonations provided an excellent opportunity to improve and refine the original cloud-tracking plan, and to experiment with different tracking methods. The use of different tracking techniques produced a variety of



data which permitted gradually increasing sophistication of the data analysis.

The results obtained with the Mark V lidar and the various observational and analysis techniques which are discussed in detail in Section IV may be summarized as follows (see also Table I):

Bravo Volume estimates of the visible cloud;

Charlie: Horizontal projection of the visible cloud boundaries,  
Relative density contours of the visible cloud,  
Relative density contours of the sub-visible cloud,  
Volume estimates of the visible cloud;

Alfa: Height and growth of cloud vs. time,  
Cloud backscatter coefficient as a function of time,  
Horizontal projections of the visible and sub-visible cloud boundary,  
Volume estimates of the visible and sub-visible clouds;

Delta: High-resolution relative density contours of the sub-visible cloud.

The maximum period for which the sub-visible cloud was observed was 30 minutes (Charlie). The maximum range at which the ~~sub-visible cloud was detected~~ was 4125m (Delta). The maximum height attained by a cloud under observation was 932 m (Bravo). Volume backscattering coefficients ranged from  $0.7 \text{ km}^{-1}$  to  $20 \text{ km}^{-1}$ , and were evaluated to a resolution of 2-dB increments (Alfa).

Spatial resolution obtained in plotting density distribution was of the order of 30 to 40 m (Delta).

## B. Conclusions

It is concluded that this program has completely attained its objectives; and the general capability of lidar in observing the dust clouds resulting from large-scale explosions is assessed as follows:

- (1) Lidar echoes can be obtained from the clouds even when they become too diffuse to be visible.
- (2) Lidar observations can provide information on the position of such echoes

in three dimensions relative to datum, with sufficient resolutions in space and time to determine the position, lateral and vertical extent, and volume of the cloud. Successive observations thus readily provide information on the cloud's rate of growth and motion.

- (3) The reflectivity per unit volume of the cloud can be measured by lidar with sufficient accuracy to infer (in general terms) the distribution of matter within the cloud. Changes therein with time due to diffusion and fallout can be monitored. (Note: It is not possible at the present time to obtain particle size and number density distributions directly from lidar observations).

The extent of these capabilities will depend upon the parameters of the lidar equipment used. In this regard, it is important to recognize that the lidar used in this program is a research instrument designed to be readily adapted for a variety of uses, and not an instrument optimized for the specific requirements of this program. The opportunity of observing a sequence of four explosions in this program made it possible to explore a variety of observing and analysis techniques which effectively cover the range of possible applications. The experience gained will be valuable in making subsequent observations of explosions with the same or similar lidar equipment. It is also of great value in determining the path to be followed in the development of optimum equipment for this purpose. Recommendations based on this experience follow.

#### C. Recommendations

##### 1. General

The ultimate capability of lidar to monitor dust clouds caused by large-scale explosions will depend upon how well the equipment can meet the requirements for information in terms of data rate and performance. The factors that are most significant in determining capability are the pulse-repetition rate and power output of the laser (to a certain extent these two factors are interrelated). How far expected progress in lidar technology can go toward meeting this information requirement cannot

be stated precisely at this time--for one thing, the exact operational requirement has not been closely defined. It is quite apparent, however, based on the experience of the current program, that considerable contributions can be made by existing equipments and those readily attainable. The steps that can be taken in the immediate future to achieve improvements can now be specified, and it is also possible to indicate the general direction that development should take.

First, however, it should be noted that interim solutions must of necessity be limited solutions. Early attention should be paid, therefore, to determining what is required of the lidar observation program in any given case. For example, the technical requirements and operation procedures necessary to determine the rate of growth in the early stages of the cloud will differ considerably from those necessary to trace density variations of the sub-visible cloud at long range.

Based, then, on a general understanding of the conditions and requirements appropriate to tracking nuclear clouds, the following recommendations are made for increasing the efficiency in future operations.

## 2. Observational Procedure

It is first necessary to establish the primary and secondary objectives of the observation on any occasion. Clear plans with readily implemented alternatives must be formulated and rehearsed. These plans should be capable of being switched or modified according to actual circumstances as they develop. Objectives should be confined to a few important items that can be done well, rather than attempting to cover too wide a range of data collection with interim equipment.

## 3. Equipment

### a. System Detection Performance

The performance of the Mark V neodymium lidar was adequate for the

fairly-close-range observations discussed in this report. To obtain longer operational ranges on clouds of similar reflectivity, higher performance is necessary. As an initial step, this can be achieved by employing a ruby laser, to take advantage of the increased sensitivity of such systems, but the use of lasers of increased power is obviously indicated. All other factors (see Eq. 3) that will increase system performance must be exploited in subsequent designs.

b. Pulse-Repetition Frequency

The pulse rate of the Mark V neodymium system (12 per minute maximum), was adequate for many of the observations made but is obviously far short of optimum. With present technology, high pulse-repetition rates cannot readily be attained with high powers. In an immediate interim approach, it is considered that if a choice has to be made between increasing performance and increasing data rate, an increase in performance is to be preferred. By using a ruby laser version of the Mark V system, in accordance with Section H-C-3-a above, a reduction in pulse-repetition frequency must be accepted (to about 1 per minute). In future developments it is necessary to achieve the highest possible pulse-repetition frequencies conducive to maintaining or improving system detection performance.

c. Data Recording

A significant increase in the firing rate may place additional demands on the method used to record the laser output signal. At the present time, the output signal resulting from each laser firing is separately recorded on the magnetic disc recorder. The present capacity of the disc is 100 recordings. However, the disc capacity can be readily increased to meet the storage of 1000 recordings.

d. Data Display

The operator of the laser should be provided with some form of data display

in order to increase his cloud-tracking efficiency. This would be particularly important in the case of a high-pulse-repetition-rate system. One possibility might be some form of (PPI) Plan Position Indicator, or range-vs. -azimuth display provided by a conventional oscilloscope using the magnetic disc recorder as buffer storage. The disc recorder would repetitively play back the data obtained during the previous few minutes of operation.

e. Lidar Pointing Angles

An improved method of recording azimuth and elevation angles of the lidar beam is necessary. One possibility is to install digital shaft-angle encoders on the azimuth and elevation axes of the lidar. The output from these encoders could be used to provide pointing-angle data for the lidar display. Consideration should also be given to incorporating an automatically programmed scanning capability.

f. Equipment Calibration

Improvements in the absolute calibration of the lidar are necessary to allow more accurate backscatter coefficient measurements to be made.

4. Analysis Techniques

In order to arrive at an accurate plot of backscatter vs. range for a given region within the cloud, it is necessary to remove the effects of attenuation suffered by the signal along the portion of the path that lies within the cloud (Eq. 2). Convenient analysis techniques capable of removing the effects of cloud attenuation should be developed to provide more accurate information regarding the density distributions within the cloud.

### III INSTRUMENTATION AND DATA FORMAT

#### A. Mark V Lidar

Two of the Institute's lidars, the Mark I (Ruby) and the Mark V (Neodymium) were available for use on this project. Although the ruby system has a maximum range greater than that of the neodymium, the latter has a significantly higher firing rate. Since tracking the cloud and mapping its internal density variations were of primary interest, the neodymium system with its higher firing rate was selected for this project.

The Mark V lidar transmitter consists of a Q-switched, neodymium-doped glass laser whose output radiation occurs in the near-infrared portion of the spectrum at a wavelength of  $1.06\mu$ . The laser is capable of producing pulsed coherent radiation of 30 Nanoseconds duration, with a peak power output of 25 Megawatts. The laser output beam divergence (beamwidth) is approximately 5.6 milliradians. Since the angular resolution of the lidar is determined by the transmitted beam divergence, collimating optics are used to reduce the beam divergence and to produce an output beamwidth of 0.35 milliradians. The corresponding spatial resolution of this beam is 0.35m at a range of 1 km. The pulse-repetition rate (PRR) of the Mark V lidar is primarily limited by the ambient air temperature, which determine the cooling rate of the laser head. For the relatively low temperatures encountered during the observations discussed here (approximately  $20^{\circ}\text{F}$ ), the maximum PRR attained was 12 pulses per minutes.

The lidar receiver consists of a 6-inch diameter Newtonian reflecting telescope, identical to the transmitter optics. An adjustable field stop at the focal plane limits the receiver acceptance angle to a maximum of 6 milliradians. A multi-layered

narrowband filter with a wavelength interval (bandwidth) of 0.01  $\mu$  is inserted in the receiver optical path to reduce the output noise level produced by solar radiation scattered into the receiver field of view. The detector consists of an RCA 7102 photomultiplier with S-1 spectral response. An optical diagram of the lidar is shown in Figure 2a.

A detailed discussion concerning lidar detection of atmospheric targets and lidar equipment design features is beyond the scope of the present report. These topics are treated extensively in References 1, 2, and 3.

Table II summarizes the pertinent characteristics of the Mark V lidar.

**TABLE II MARK V LIDAR CHARACTERISTICS**

<u>Transmitter</u>	
Laser	Neodymium-doped glass
Wavelength	1.06 $\mu$
Beamwidth	0.35 Milliradian
Optics	6 inch f/5 Newtonian reflector
Peak power output	25 Megawatts
Pulse length	30 Nanoseconds
Q-switch	Rotating prism
<u>Receiver</u>	
Optics	6 inch Newtonian reflector
Field of view	3.0 Milliradian (normal setting)
Pre-detection filter wavelength interval	0.01 $\mu$ (100 $\text{\AA}$ )
Detector	RCA 7102 Photomultiplier (S-1 cathode)
Post-detection Filter bandwidth	6 GHz

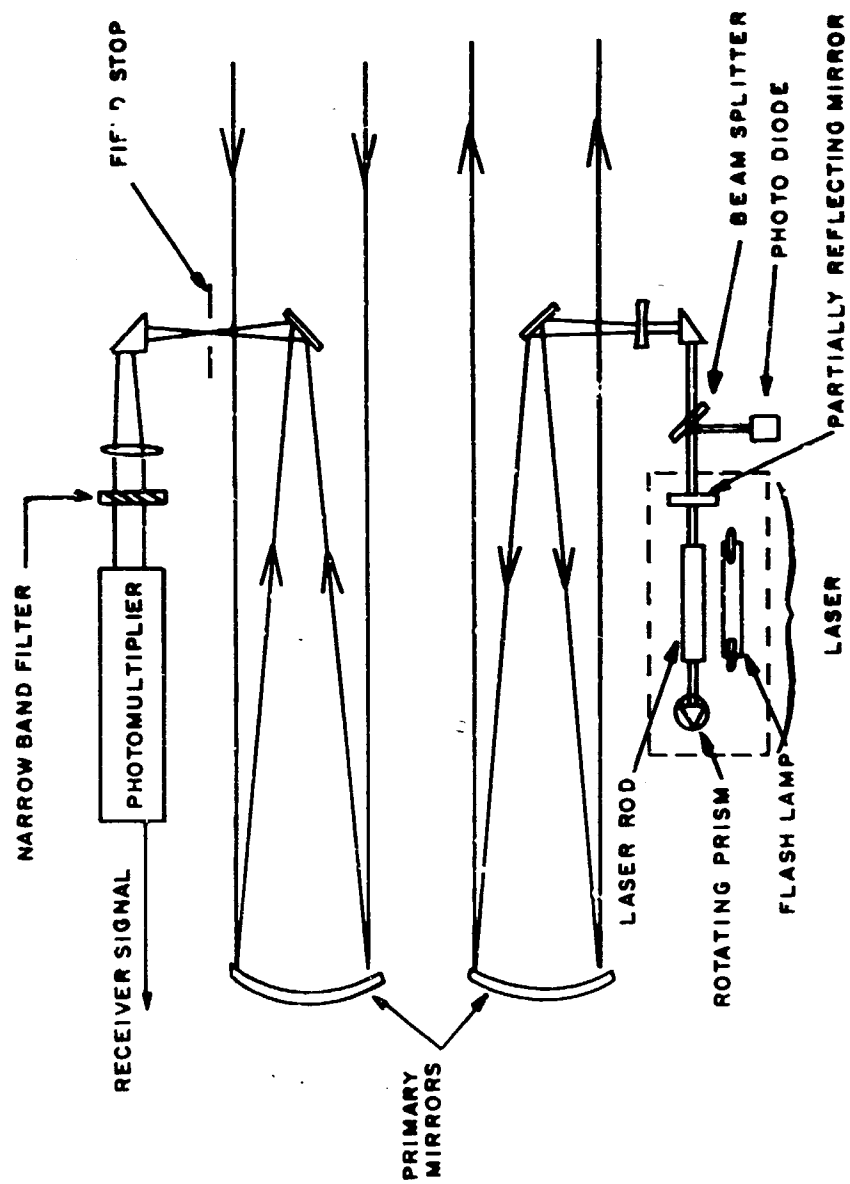


FIG 2a MARK V LIDAR OPTICAL DIAGRAM



## **B. Electronics and Data Recording Equipment**

The major electronic components of the lidar and the data recording system are illustrated in block diagram form in Figure 2b. A compressed air-driven turbine rotates the laser Q-switching prism at 500 revolutions per second. Upon receipt of a fire signal, the synchronizing generator triggers the flash lamp in step with a signal from the rotating prism. A capacitor bank charged to 3 KV supplies energy for the laser flash lamp. A trigger diode senses the occurrence of the laser pulse and produces a trigger to start the data recording equipment. The output of the photomultiplier in the lidar receiver is fed to a pulse amplifier having a logarithmic transfer function, and then to a video disc recorder; which was used as the primary method of storing the lidar output signal. The output of the video recorder is applied to a Tektronix type 555 oscilloscope, the display of which was visually monitored during the cloud tracking. A Polaroid recording camera mounted on the oscilloscope facilitated the initial alignment of the equipment, and was available to photograph the lidar return signal in the event of a failure of other recording equipment.

The video disc serves two purposes:

- (1) To record the receiver output signal produced by each lidar firing for playback and analysis at a later time;
- (2) To play back the recorded signal repetitively immediately after the lidar firing, for visual monitoring during cloud tracking.

An independent back-up system consisting of a 35-mm recording camera mounted on a second oscilloscope automatically photographed each lidar trace.

The Mark V lidar was situated at the cloud-tracking station on the Pre-GONDOLA I test site, and the electronic data-recording equipment was housed in a nearby instrument shelter. A telephone line between the lidar and the instrument shelter facilitated communication between these two points during the cloud tracking. An audio tape

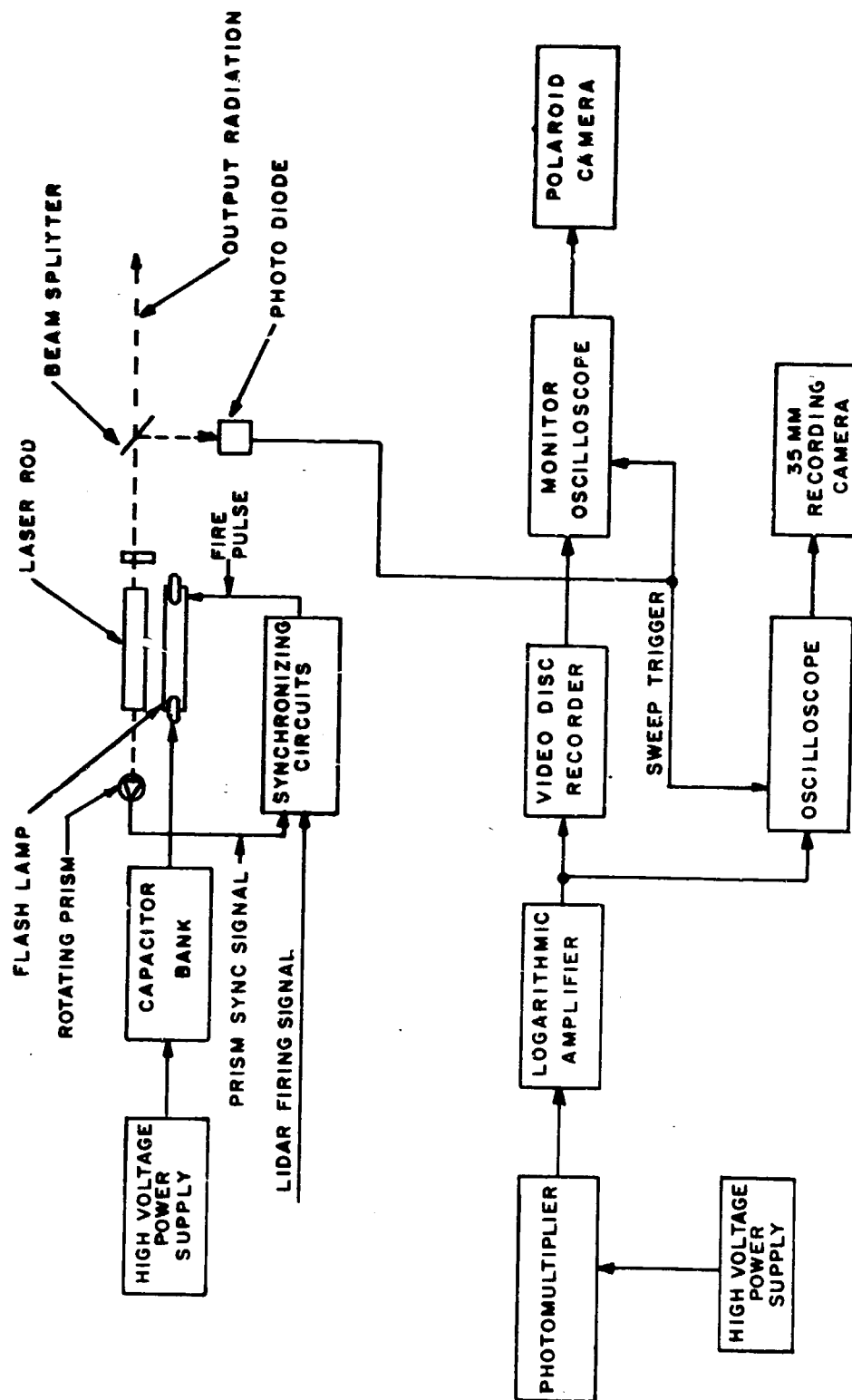


FIG. 2b BLOCK DIAGRAM OF THE MARK V LIDAR ELECTRONICS

recorder connected to the telephone party line connecting the lidar team members was used to record various equipment settings and lidar pointing angles, as well as a running commentary on the growth and motion of the cloud.

A 35 mm camera loaded with Kodachrome II film was attached to and coaligned with the lidar for Shot Delta and a series of reference photographs were made .

### C. Data Format

Figure 3 illustrates a group of typical lidar return signals, whose format is similar to a conventional radar "A scope". That is, the return signal amplitude (logarithmic scale) is displayed as a function of slant range.

The sharp increase and gradual decay of signal amplitude (called the near-field return), which occurs at approximately 150 to 800 meters slant range, is produced by energy backscattered from the clear atmosphere. Figure 4 illustrates the geometry of the transmitter beam and receiver field of view, which influences the near-field return. At very close ranges the receiver output increases as the beams gradually merge, and then falls as the range of the particles producing the backscatter increases.

The basic data for this report consist of 355 lidar "A-scope" recordings showing signal amplitude vs. slant range along with the corresponding azimuth and elevation pointing angles and the time of each laser firing. From the basic data, the height above ground zero and the plan range of any selected point on a particular lidar return can be determined along with the return signal amplitude for that point. By considering a group of lidar recordings produced when the lidar was scanned across the cloud, an estimate of the shape and extent of the cloud can be obtained, and an estimate made of its volume. The specific analysis techniques used to reduce the raw data will be described in the next section.

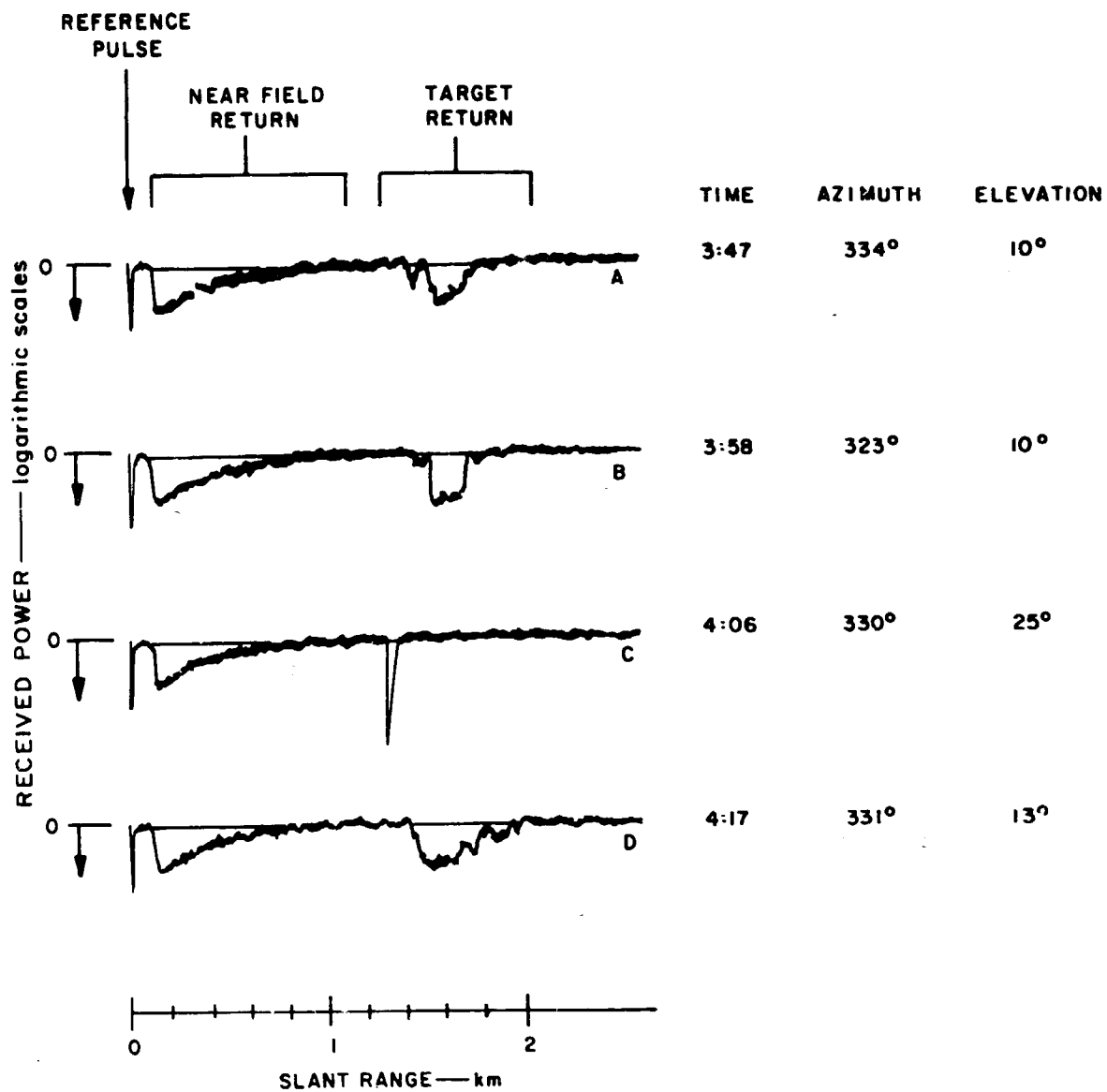


FIG. 3 TYPICAL LIDAR RETURN SIGNALS—ALFA EVENT  
(See also Fig. 26)

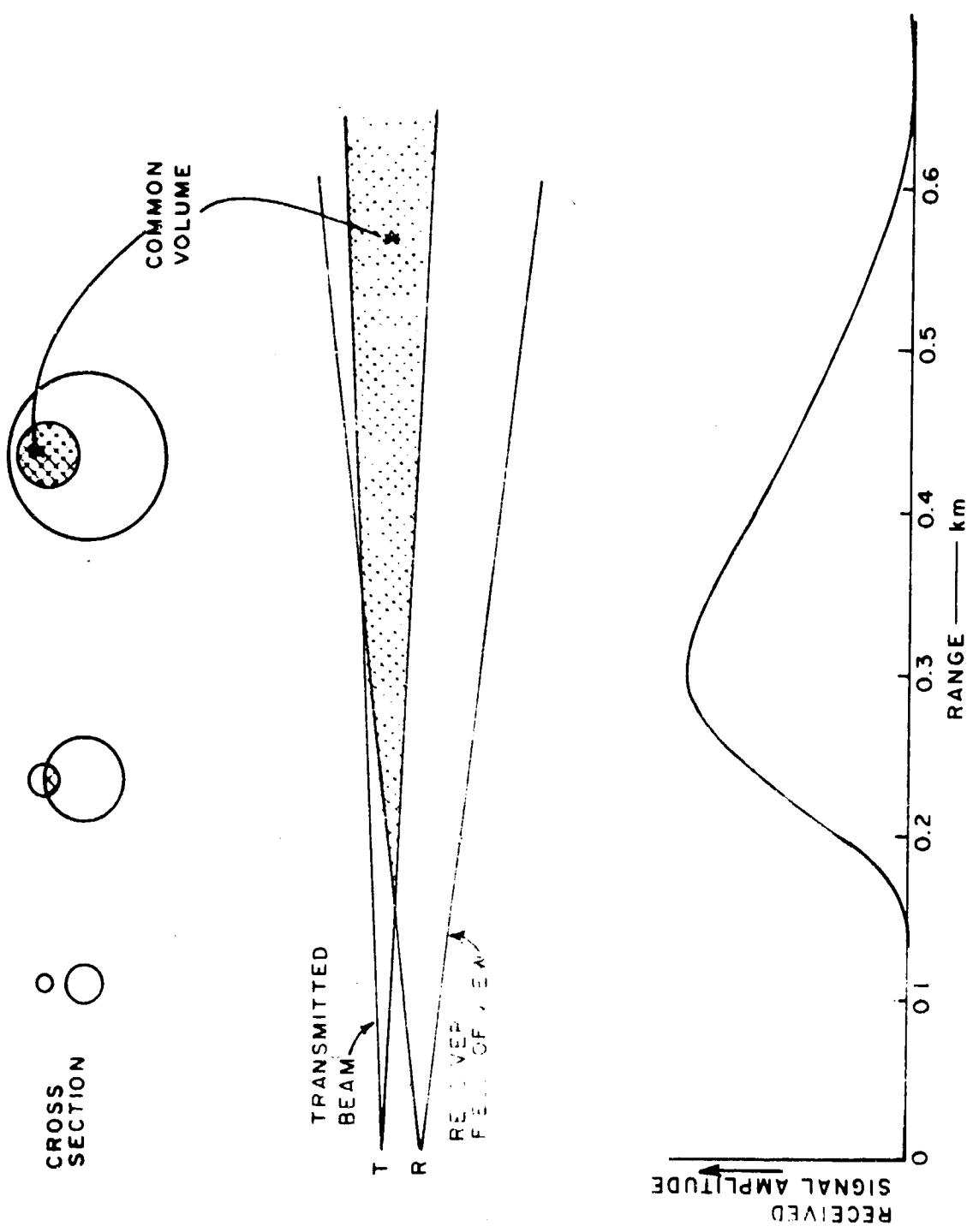


FIG. 4 LIDAR BEAM GEOMETRY

#### IV DETAILED DISCUSSION

##### A. Shot Bravo, 25 October 1966

For this shot, the lidar was positioned at the cloud-tracking station on a low (0.6 meter high) platform especially constructed for this purpose. At this location, the elevation of the lidar was 62.2 meters above Bravo surface ground zero (SGZ). An azimuth stop had been secured to the platform to physically limit the traverse of the instrument so that it could not be aimed in the direction of the Control Point.

The operation plan for this shot, which had been rehearsed the previous day, was to employ the full, four-man SRI team in the following way.

An observer was to aim the lidar toward selected regions of the visible cloud, an outline sketch of which a second observer had made on a large data pad. Upon confirmation that the field was clear of aircraft, the firing signal was given to the data recorder located in the shed, who controlled the lidar firing trigger. Immediately after firing, the azimuth and elevation angles were read off verbally by a third observer and the point of the cloud toward which the lidar was fired indicated on the sketch.

##### 1. Cloud Tracking

This shot, which detonated promptly at 10:00 AM MST, occurred under clear sky and light NNW wind conditions. Visibility was over 20 miles. The wind was veering slowly; about 1/2 hour before  $T_0$  it was from the northwest, which, if it had not veered further to the north, would have blown the cloud directly over the lidar observation point.

The first lidar shot was fired about 2 minutes after detonation; the delay was needed for the helicopter to clear the firing sector. After about ten shots the cloud had drifted in between the lidar and the Control Center and it was not possible to traverse the instrument farther to the south to observe the cloud because of the safety

stop. The Safety Officer agreed to removal of the stop because the lidar was being aimed at an elevation angle well above the horizontal and accordingly presented no possible hazard to persons on the ground.

Firing continued toward the visible cloud, which now resembled a small, tenuous, fair-weather cumulus, until it became occluded by the equipment shed, at about  $T_0 + 10$  minutes. While the cloud could still be plainly seen for another 5 or 6 minutes, the lidar could not be aimed at it. A few shots were made after  $T_0 + 20$  to the south of the shed in hopes that some portions of the cloud had drifted into view, but no echoes could be detected.

The tracking operation, in general, worked well and without major difficulty. The lidar could be fired at about 15-second intervals under this plan, the major portion of the time being required to read off the firing angles.

There is no doubt whatsoever that, but for the mischance of the cloud's drifting behind the equipment shed, it could have been tracked for at least an additional five minutes and possibly even ten or fifteen more minutes and some observations obtained of the sub-visible stages. However, valuable experience was gained and certain changes were incorporated in the operation plans which contributed substantially to success of the subsequent detonations.

Interference in the form of spurious trigger signals occurring at random times was experienced before and during the cloud tracking. The occurrence of this interference seemed to correlate with the movements of motor vehicles in the local area. The only effect of the interference was to produce premature triggering of the data-recording equipment. While this effect was annoying, it did not impede the acquisition of lidar data. Additional shielding of the signal and trigger leads between the lidar and the data display significantly reduced the occurrence of this interference during

the remaining three events.

## 2. Data Analysis

The raw data were analyzed to obtain volume estimates vs. time of the visible cloud. These estimates were accomplished in the following way. The data from each run\* were analyzed to obtain the locations of the cloud boundaries in three-dimensional space. These boundaries were connected by best-fitting plane surfaces to form a prismatoid,\*\* the value of which is readily calculated. Volume estimates for each of 6 runs are presented in Figure 5. These estimates are rather erratic, because a significant portion of the cloud was obscured during many of the observations. During Run 2, for example, over half of the visible cloud was beyond the azimuth limits of the safety stop. During Runs 5 and 6, a major portion of the cloud was obscured by the equipment shed.

### B. Shot Charlie, 28 October 1966

Between shots Bravo and Charlie an excellent wooden tower about 4.6 meters high was set up at the cloud-tracking station and the lidar and associated equipment positioned upon it. For this shot, the lidar was at an elevation of 64 meters above SGZ.

The operations plan for Charlie was very similar to that of Bravo, with some minor changes in data-recording procedures to eliminate superfluous information and further reduce the interval between lidar firings.

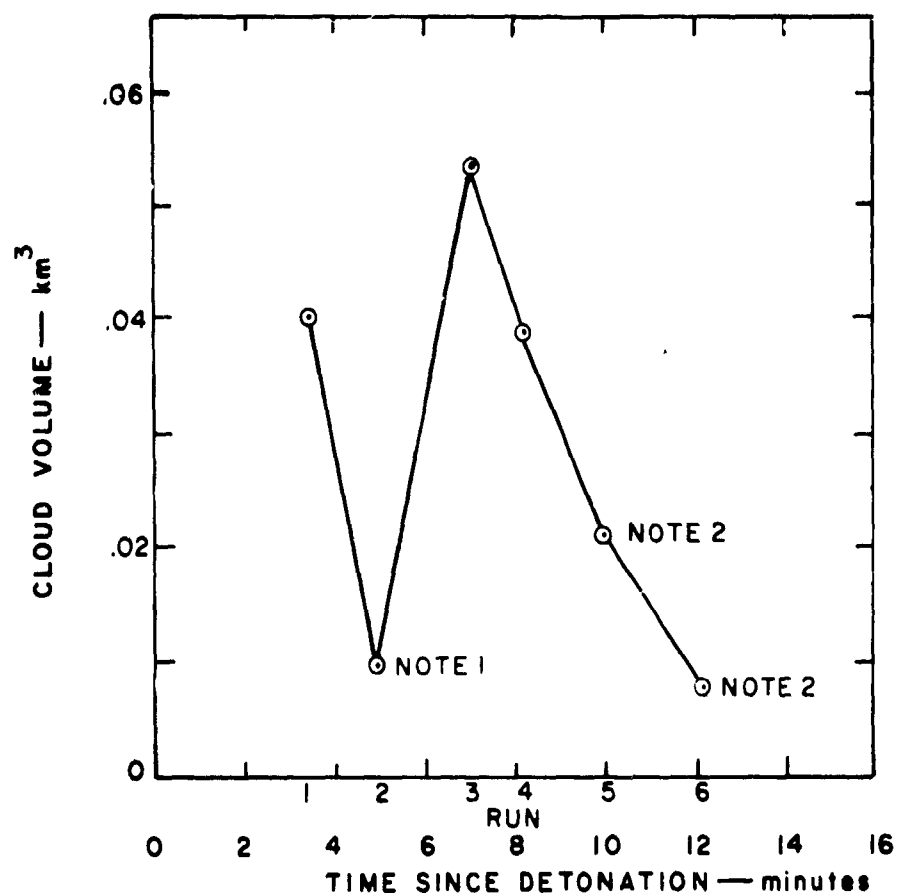
The detonation was postponed for two hours because of technical difficulties in

---

\* For the Bravo event, a run consisted of an average of 5 lidar shots, for each aimed near the boundaries of the visible cloud.

\*\* A solid having parallel base and top consisting of three or four sides; the lateral faces are composed of either triangles or trapezoids.





NOTE 1: PORTION OF CLOUD BEYOND AZIMUTH LIMITS OF SAFETY STOP

NOTE 2: PORTION OF CLOUD OBSCURED BY EQUIPMENT BUILDING

FIG. 5 VOLUME ESTIMATE OF THE VISIBLE CLOUD - BRAVO

connection with arming the charge. During this interval checks were made of the performance of the lidar about every fifteen minutes to ensure that all was in readiness. The wind was very light, almost calm, from the north--about 2 to 4 mph. There were scattered cumulus clouds at one kilometer altitude above the lidar.

#### 1. Cloud Tracking

Shot Charlie produced a substantial dirt column which appeared to have two towers, and its steam cloud completely evaporated within four or five minutes after the detonation. The dark dust cloud slowly expanded as it drifted southward toward and to the west of the lidar. About 15 minutes after detonation the dust cloud limits were quite difficult to discern visually although the principal bulk of the cloud was still apparent. About 20 minutes after detonation no portion of the cloud was visible, although the lidar could still be aimed without difficulty toward its remnants because by this time it was only a relatively short distance away and was moving very slowly. A predetermined plan was instituted for establishing the limits of the cloud by firing at 10-degree azimuth intervals from south to north across the sky where the cloud was known to be located. Firing continued until  $T_0 + 30$  minutes at which time there still remained a very slight echo, but little further information to be obtained.

#### 2. Data Analysis

The horizontal projection of the visible cloud boundary during various stages of its life are presented in Figures 6 through 11. These figures illustrate the cloud growth and its motion over the ground referenced to the lidar and to ground zero.

The position of the radial lines originating at the lidar and intersecting the cloud boundaries indicates the lidar azimuth angle for a given observation. The corresponding elevation angle is noted at the end of the azimuth line.

The horizontal projections were not obtained by noting the slant range at which

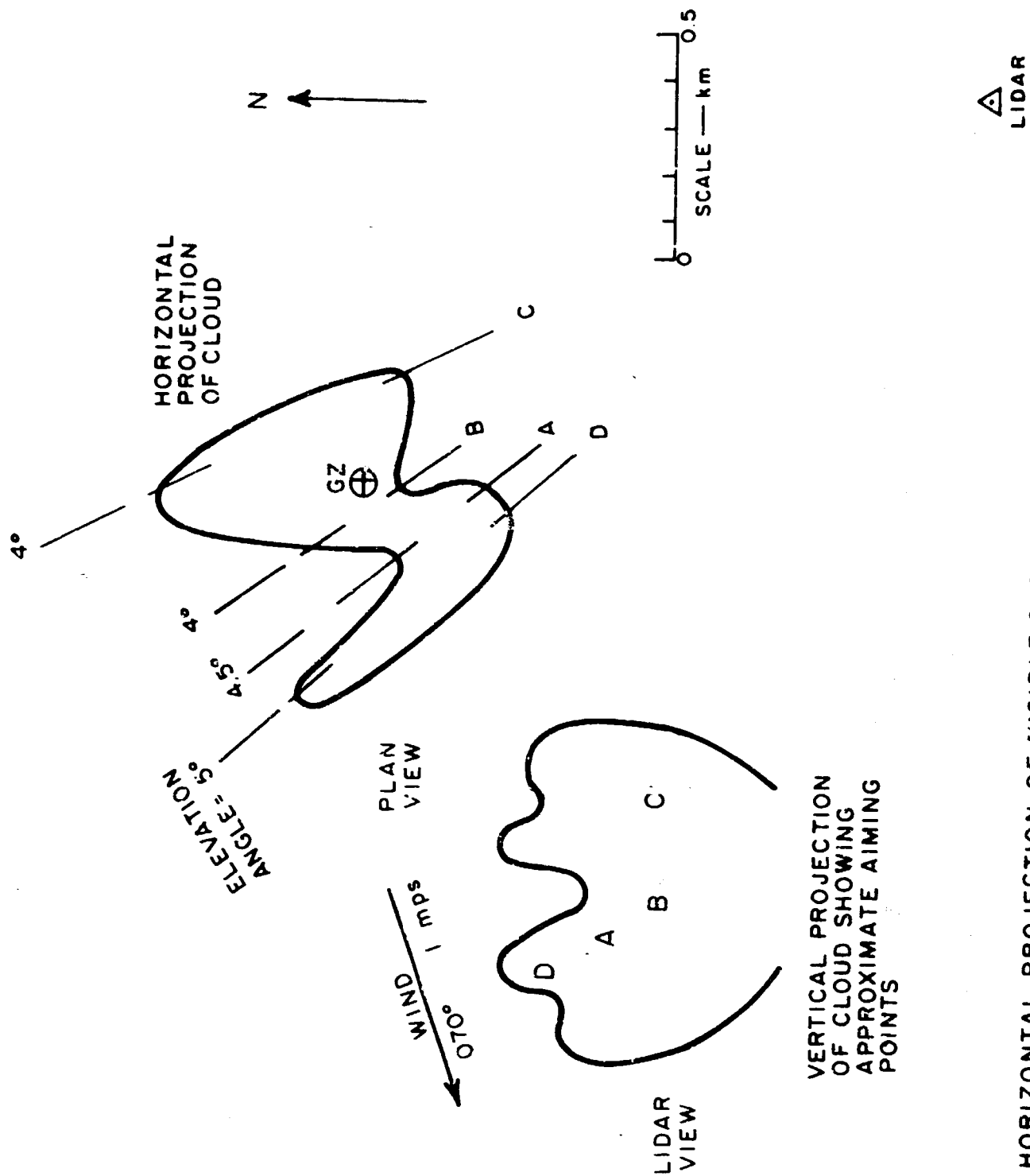


FIG. 6 HORIZONTAL PROJECTION OF VISIBLE CLOUD BOUNDARIES  
—CHARLIE; TIME: 1:58 to 2:52 min.



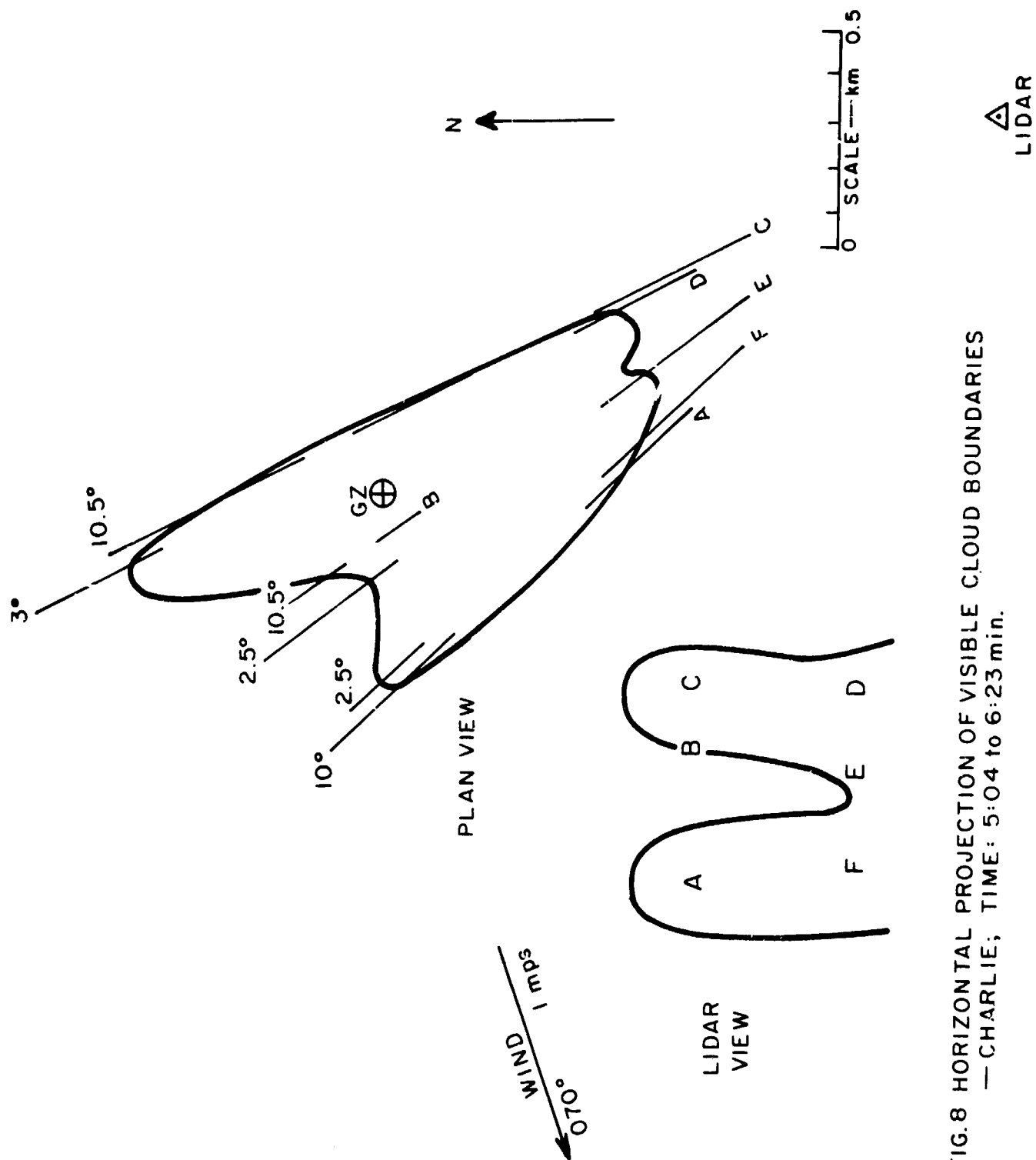
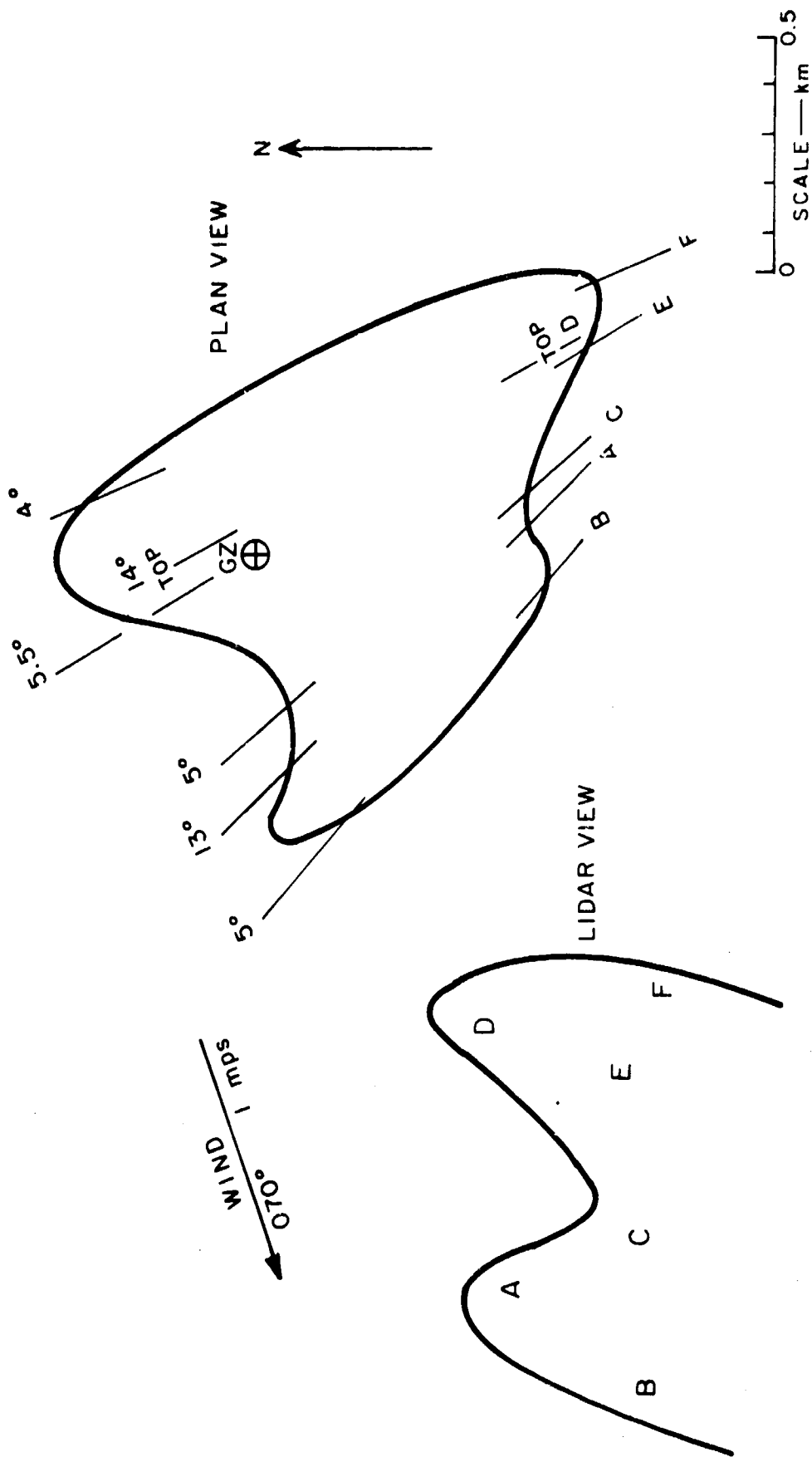


FIG. 8 HORIZONTAL PROJECTION OF VISIBLE CLOUD BOUNDARIES  
— CHARLIE; TIME: 5:04 to 6:23 min.



△ LIDAR

FIG.9 HORIZONTAL PROJECTION OF VISIBLE CLOUD BOUNDARIES  
—CHARLIE; TIME: 6:55 to 8:21 min.

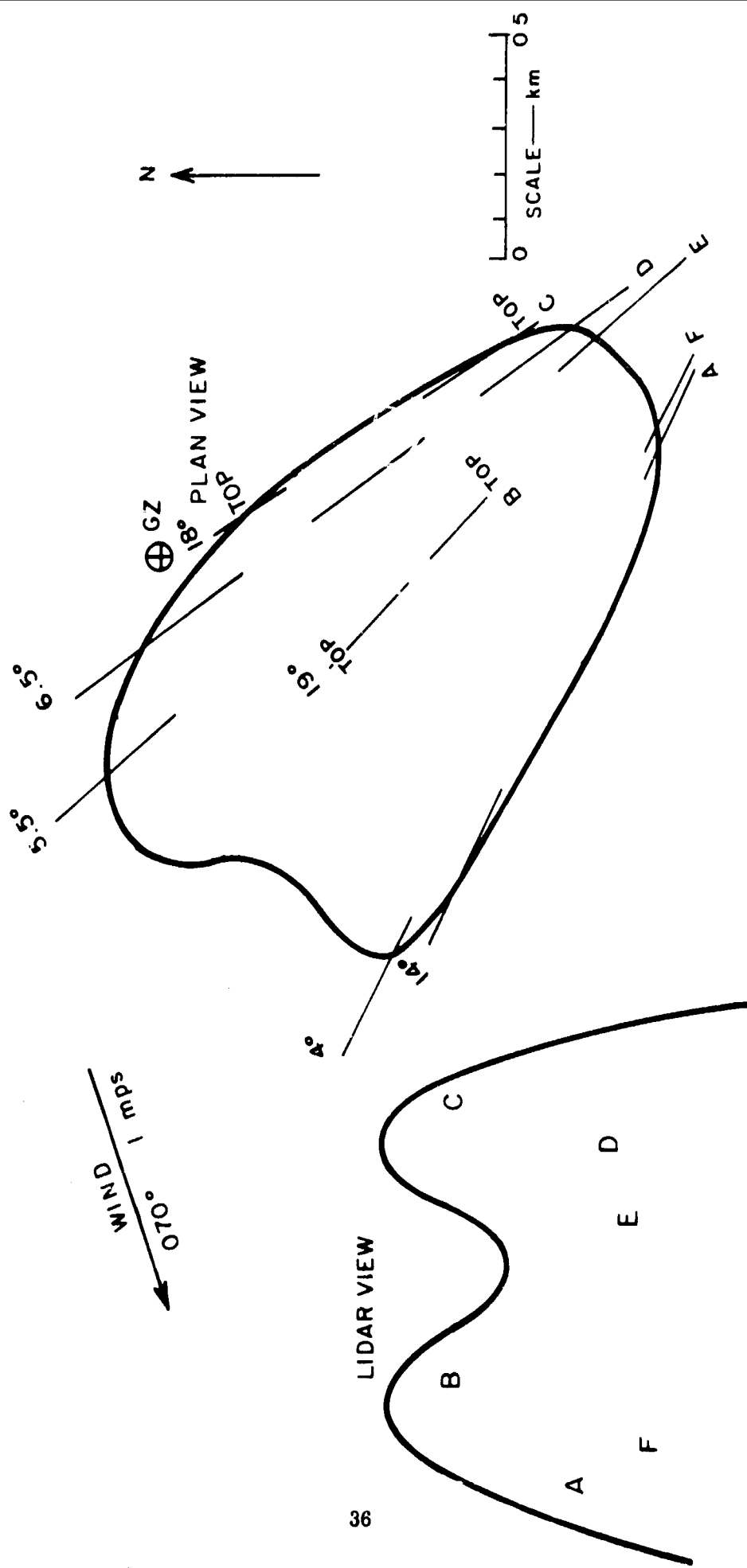


FIG. 10 HORIZONTAL PROJECTION OF VISIBLE CLOUD BOUNDARIES  
— CHARLIE; TIME: 9:21 to 10:37 min.

△  
LIDAR

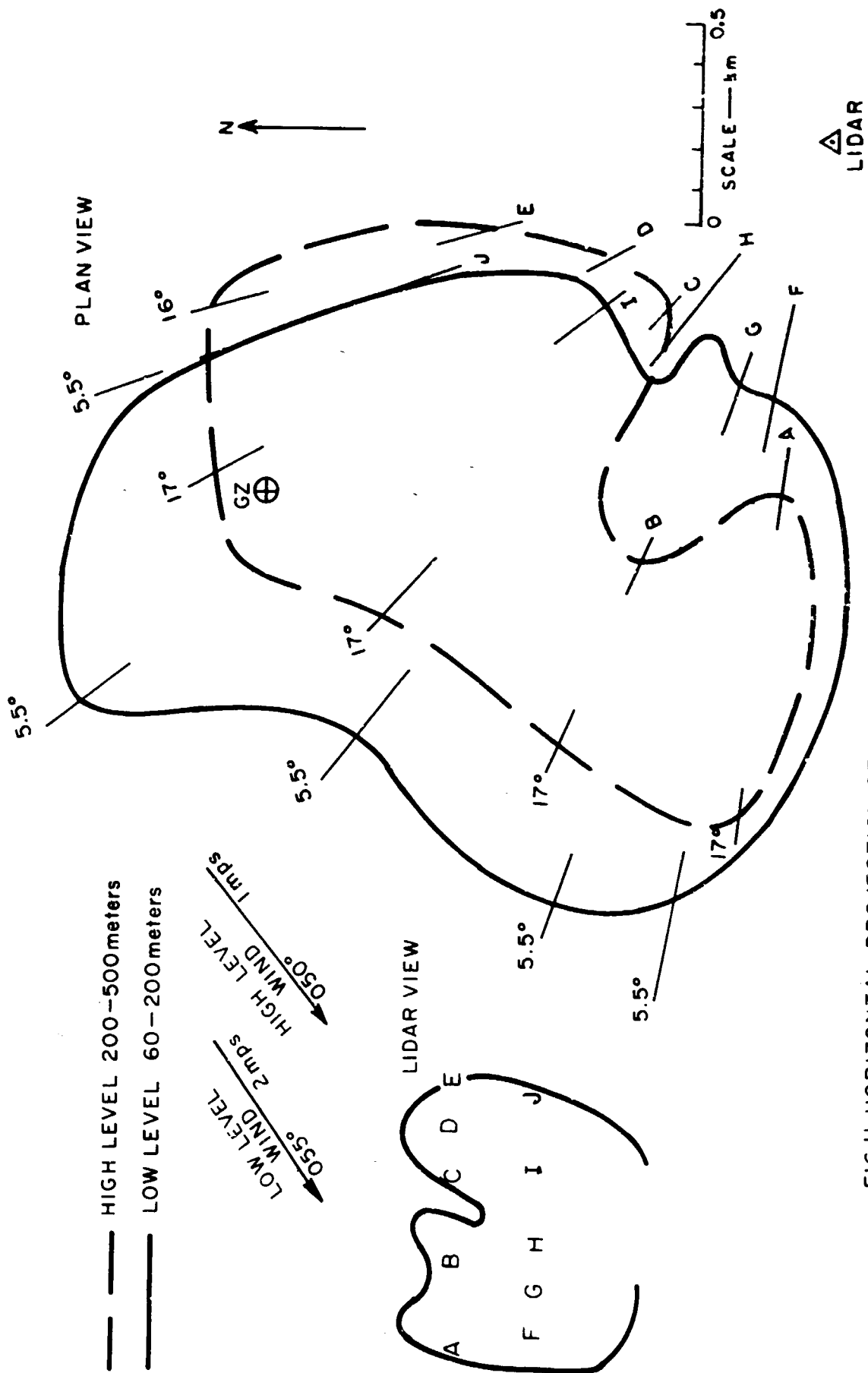


FIG.11 HORIZONTAL PROJECTION OF VISIBLE CLOUD BOUNDARIES  
— CHARLIE; TIME: 11:15 to 13:07 min.



the lidar beam enters and leaves the cloud, and computing the corresponding value of ground range. The two values of ground range for each azimuth angle define the radial limits of the cloud.

The wind direction and velocity in meters per second (mps) are indicated on each figure.

The vertical projection of the visible cloud (marked "lidar view") is included in each of the above figures. These vertical projections are approximate, since they were obtained from the observers' sketches of the cloud shape, and not from the lidar data. The only purpose of these projections is to indicate the approximately position of the lidar aiming points, which are identified by letters.

A vertical profile of relative density variations within the visible cloud is illustrated in Figure 12. The values of the various contours are expressed in decibels\* referenced to the return obtained from a clear atmosphere. Thus, 0 dB corresponds to a contour where the return signal is equal to the return from a clear atmosphere, 6 dB corresponds to a 4:1 increase in the return signal, etc.

The boundaries of the sub-visible cloud and the relative distribution of material within it are illustrated in Figure 13, where each contour represents a 3-dB or 2:1 change in signal level. The figure shows the density variations existing near the base of the cloud during the time interval between  $T_0 + 19:49$  and  $T_0 + 21:30$  minutes.

A volume estimate vs. time of the visible cloud is presented in Figure 14. The method described in shot Bravo was used to obtain the cloud volumes.

¶ Figure 15 shows horizontal cross sections of the sub-visible cloud taken at  $5^\circ$ .

---

\* Decibels are here used as expressions of power ratio:  $n \text{ db} = 10 \log \frac{P}{P_{\text{reference}}}$ , where P is power of returned signals.

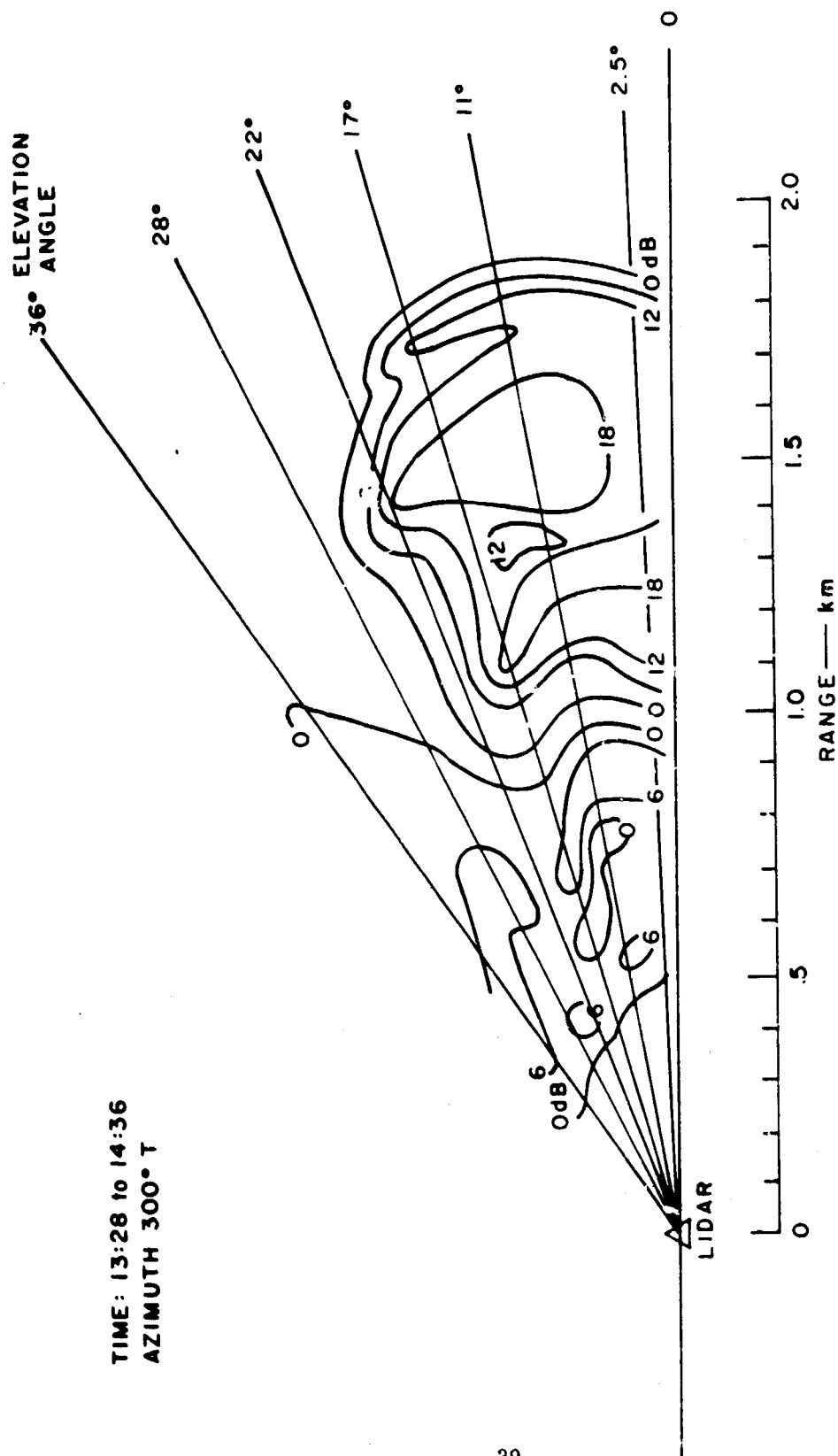


FIG.12 RELATIVE DENSITY VARIATIONS OF THE VISIBLE  
CLOUD — VERTICAL PROFILE, CHARLIE

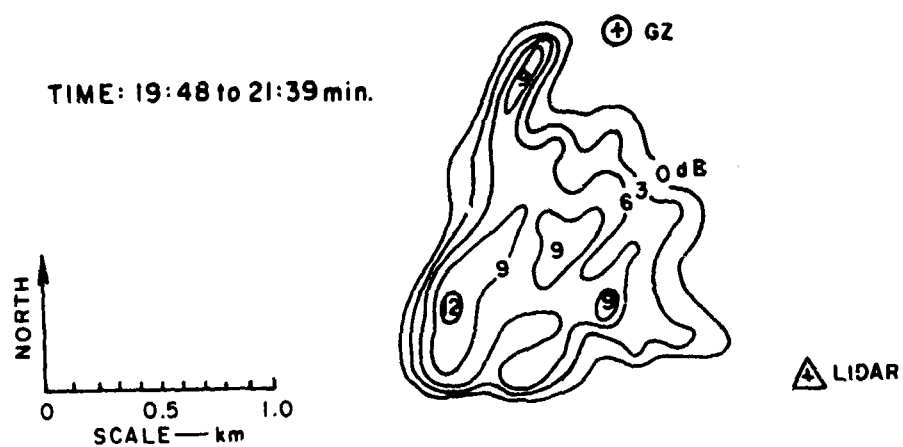


FIG. 13 RELATIVE DENSITY VARIATION OF THE SUB-VISIBLE CLOUD — HORIZONTAL PROFILE — CHARLIE

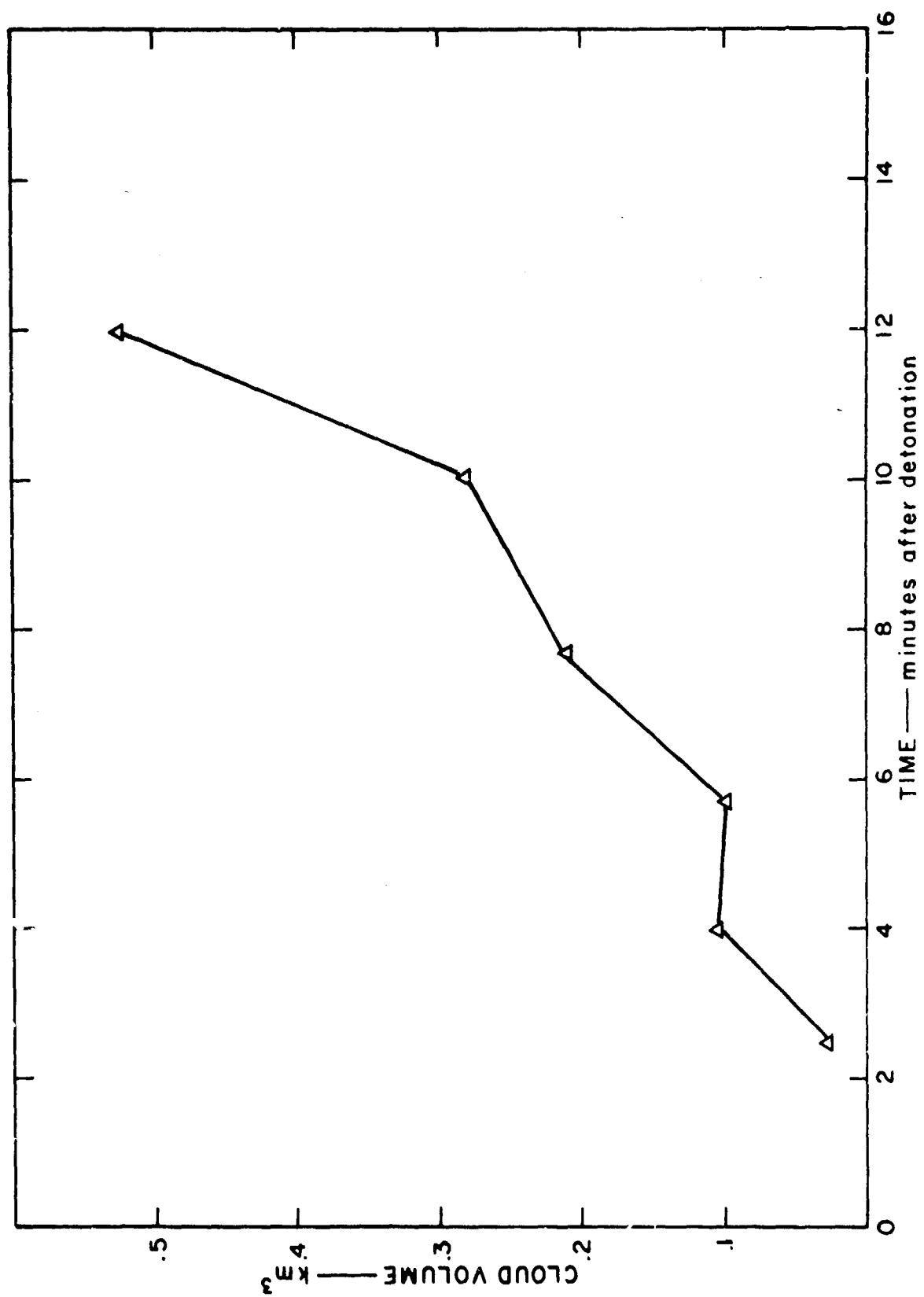


FIG. 14 VOLUME ESTIMATE OF THE VISIBLE CLOUD — CHARLIE

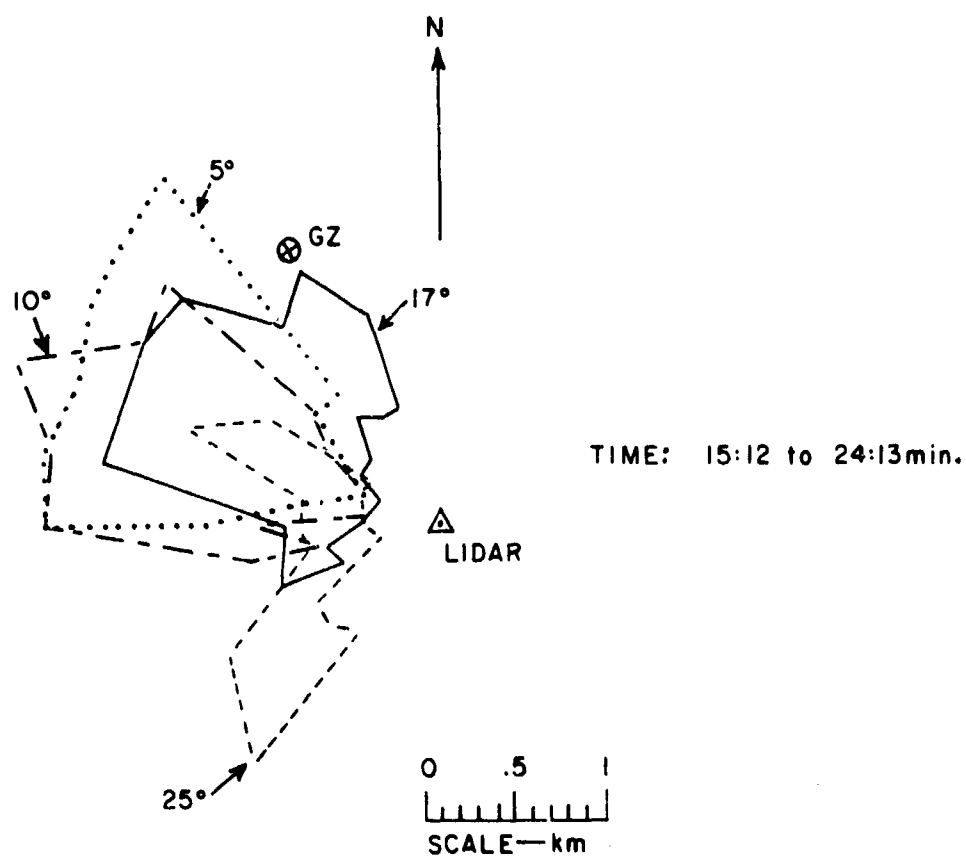


FIG.15 HORIZONTAL CROSS SECTION OF THE SUB-VISIBLE CLOUD AT 5°, 10°, 17°, AND 25° ELEVATION ANGLES — CHARLIE

10°, 17°, and 25° elevation angles during the time interval  $T_0 + 15:12$  to  $T_0 + 24:13$  minutes. The calculated volume of the cloud based on these data is 0.696 km<sup>3</sup>, which is in good agreement with the data of Figure 14. The angular relationship of these various lidar shots is shown in Figure 16.

C. Shot Alfa, 1 November 1966

1. Cloud Tracking

a. The initial cloud was tall and narrow with a top like a natural cloud. This top rose rapidly to reach a maximum height of approximately 665 meters above SGZ by  $T_0 + 4$  minutes and then lowered slightly as it spread out and dispersed by about  $T_0 + 7$  minutes. (The rate of ascent is shown in Figure 17.)

During this period the width of the cloud as seen from the lidar site grew from approximately 100m at  $T_0 + 2$  minutes to approximately 400m at  $T_0 + 6$  minutes (See Figure 18). Meanwhile the maximum radial depth as seen from the lidar site increased from 400m at  $T_0 + 2$  minutes to approximately 550m at  $T_0 + 6$  minutes. The cloud was thus slightly elongated along an approximately SE-NW axis (see Figure 19).

During this growth the highest point appeared to remain in the vicinity of SGZ, although at the lower levels (265 to 465m) the cloud drifted away to the northwest. This resulted in an overhang with the highest point being nearer the lidar than the main cloud.

By  $T_0 + 5$  minutes, as the cap cloud started to disperse, the dust cloud falling away from it to the west became more apparent and progressively more measurements were made on this portion of the cloud as the cap cloud disappeared.

b. The Sub-Visible Cloud

By  $T_0 + 7$  minutes very little, if any, of the cap cloud remained, and here-

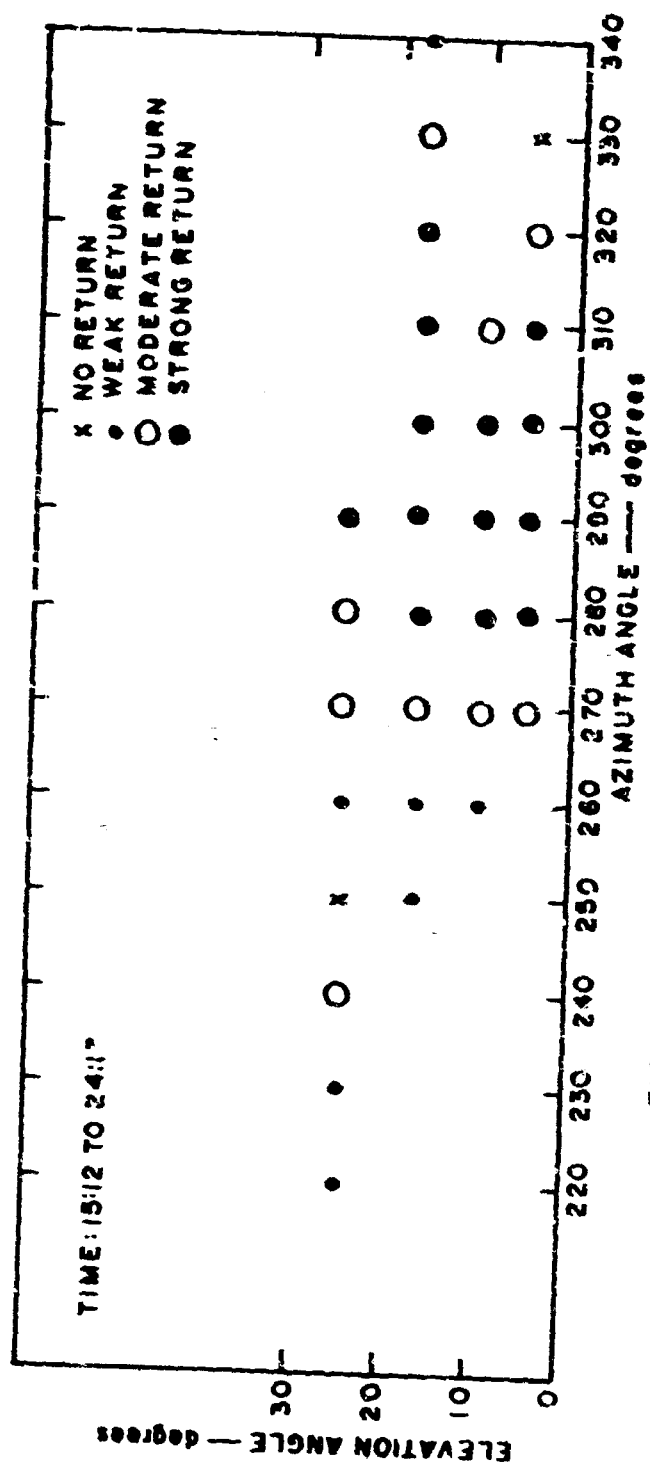
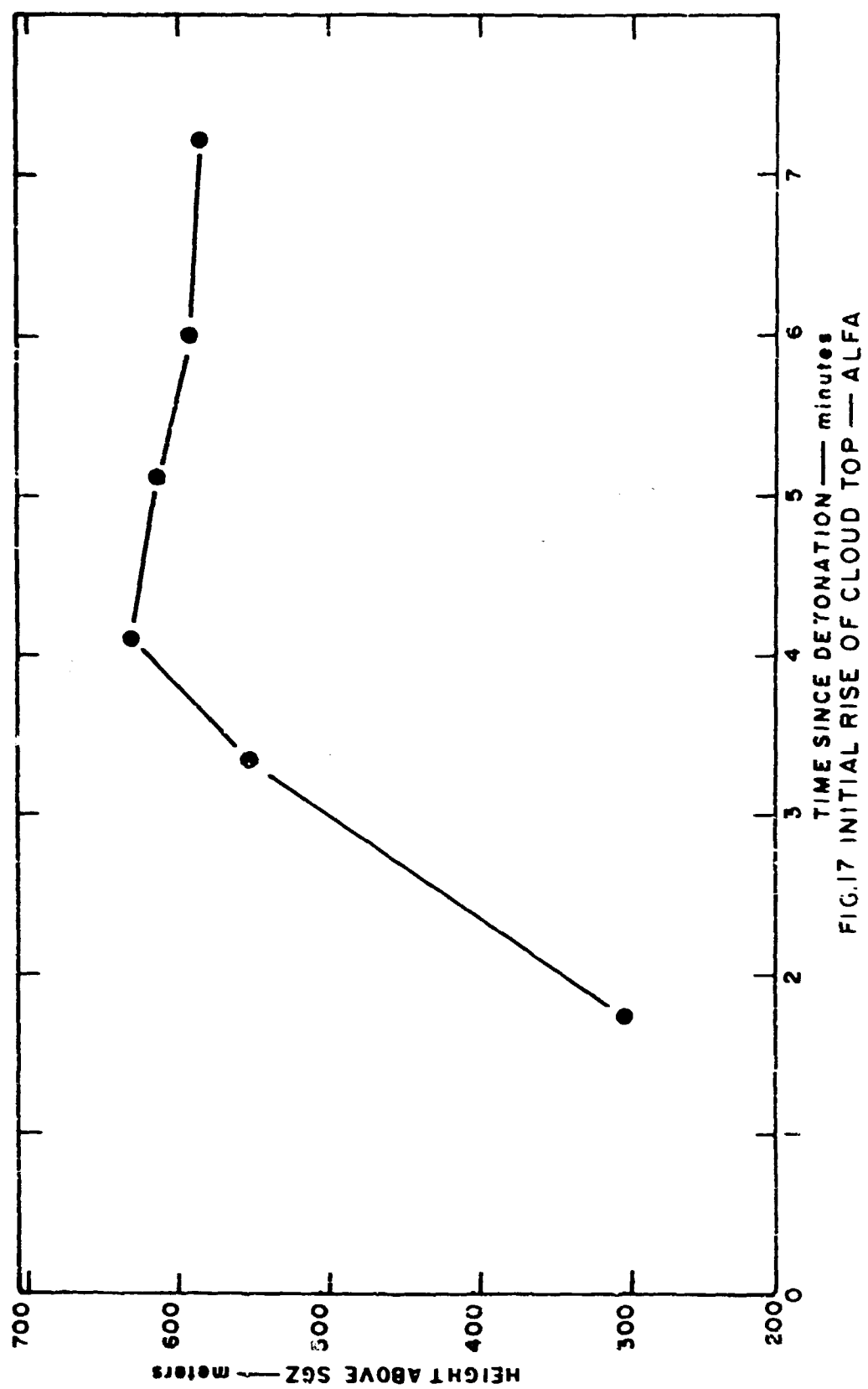


FIG. 16 ANGULAR RELATIONSHIP OF THE LIDAR SHOTS  
OF FIG. 15 — CHARLIE





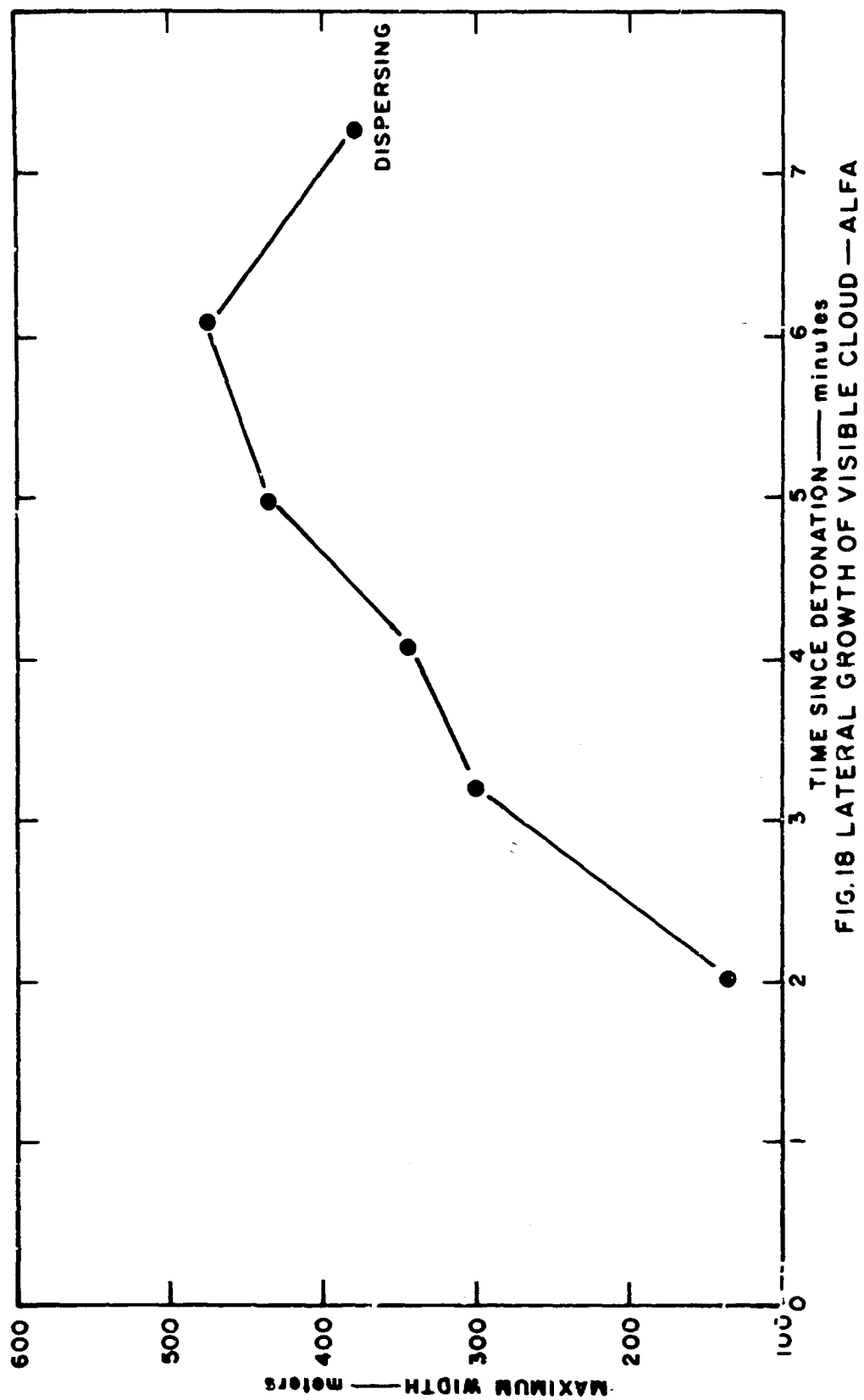


FIG.18 LATERAL GROWTH OF VISIBLE CLOUD —ALFA

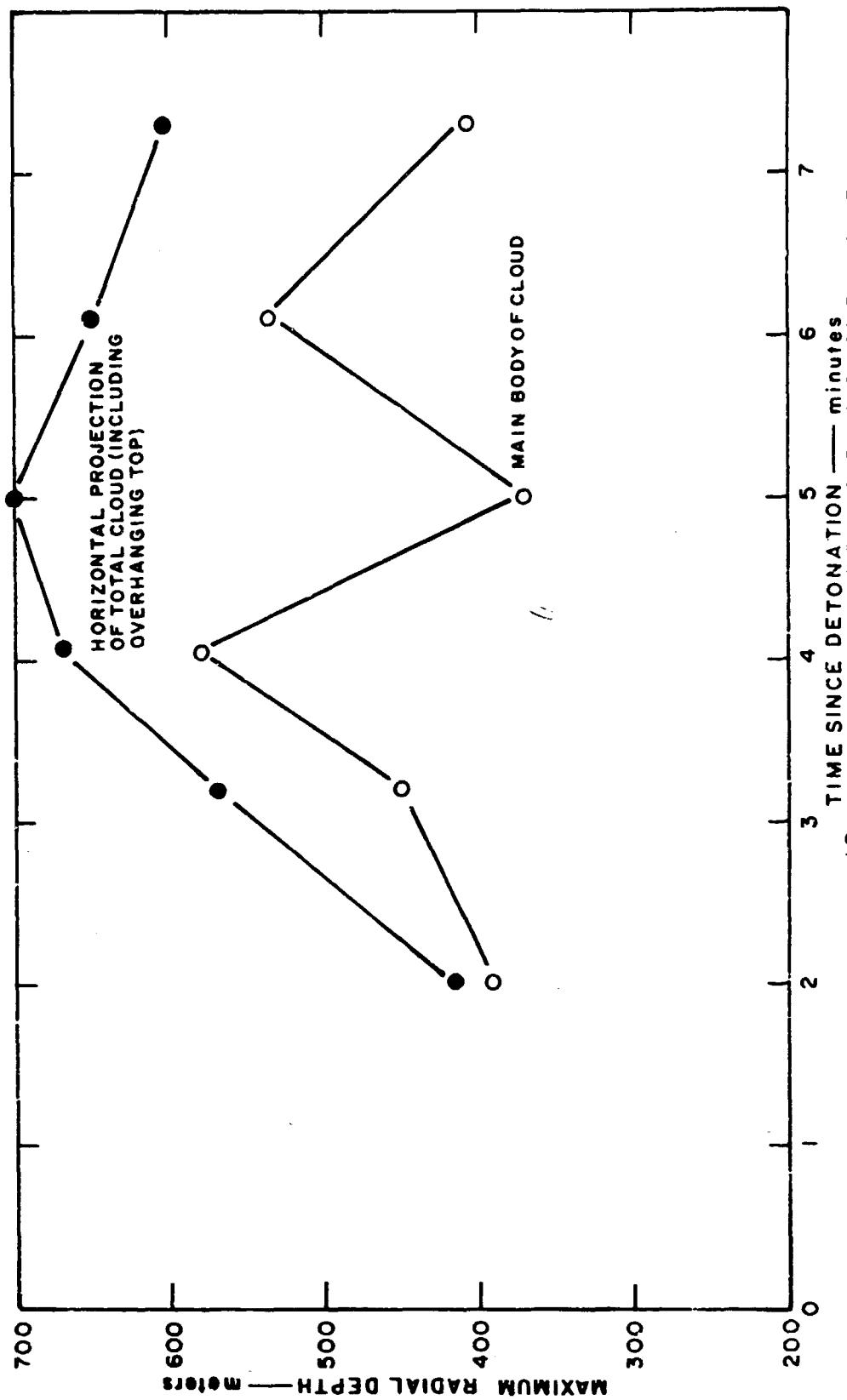


FIG. 19 RADIAL DEPTH OF VISIBLE CLOUD—ALFA

after measurements were made through the tenuous veil of dust. In the early stages the lidar was aimed by reference to the vestigial cloud, and this will bias the measurements in the lateral sense, since, in the radial direction the lidar detected dust far too thin to be visible. In the latter stages the lidar detected a wide range of dust concentrations outside the visible cloud boundaries, when the lidar was pointed without reference to visual indications, the cloud was detected laterally over a wider area. There are clear indications, however, that the dust cloud was elongated (by wind shear) along a SE-NW axis, as it drifted northwest and extended in that direction.

The lateral and radial growth of the dust cloud during this stage is shown in Figures 20 and 21. In general, from approximately  $T_0 + 9$  minutes, when the cloud was about 250m wide and some 900m deep, it grew so that by  $T_0 + 14$  minutes it was some 450m wide and some 1300m deep. Echoes were obtained at heights of 365 to 515m during this phase, although there is no way of knowing how near the top of the cloud the beam passed.

From about  $T_0 + 14$  minutes, information on the dust cloud became uncertain owing to the difficulty of adequately scanning the volume to detect the sub-visible target. However, echoes were obtained from the remains of the dust cloud as late as  $T_0 + 18$  minutes to a maximum of 2300m plan range (height 365 to 465m).

At  $T_0 + 14:30$  minutes, in scanning the sub-visible cloud, observations were made to the north of where the main dust cloud had been observed. Weak echoes were obtained from an extensive area (approximately 500m wide and 1200m deep) roughly due north of SGZ, starting some 400m from it. These echoes weakened further but persisted until approximately  $T_0 + 20$  minutes, when returns were obtained beginning at approximately 1000m and extending to some 2200m plan range heights 465 to 565m). Although there is a chance that this group of echoes came

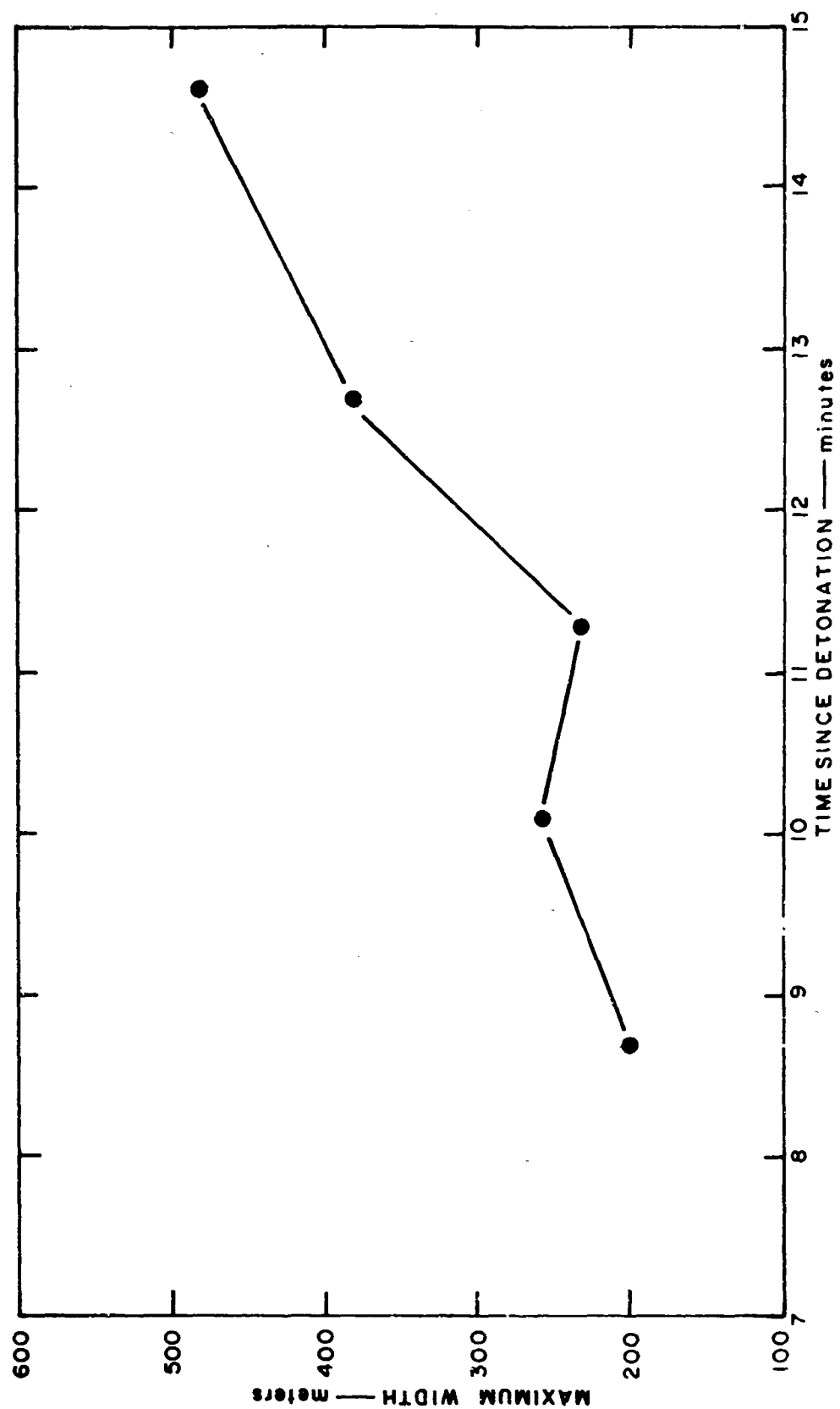


FIG.20 LATERAL GROWTH OF SUB-VISIBLE CLOUD — ALFA

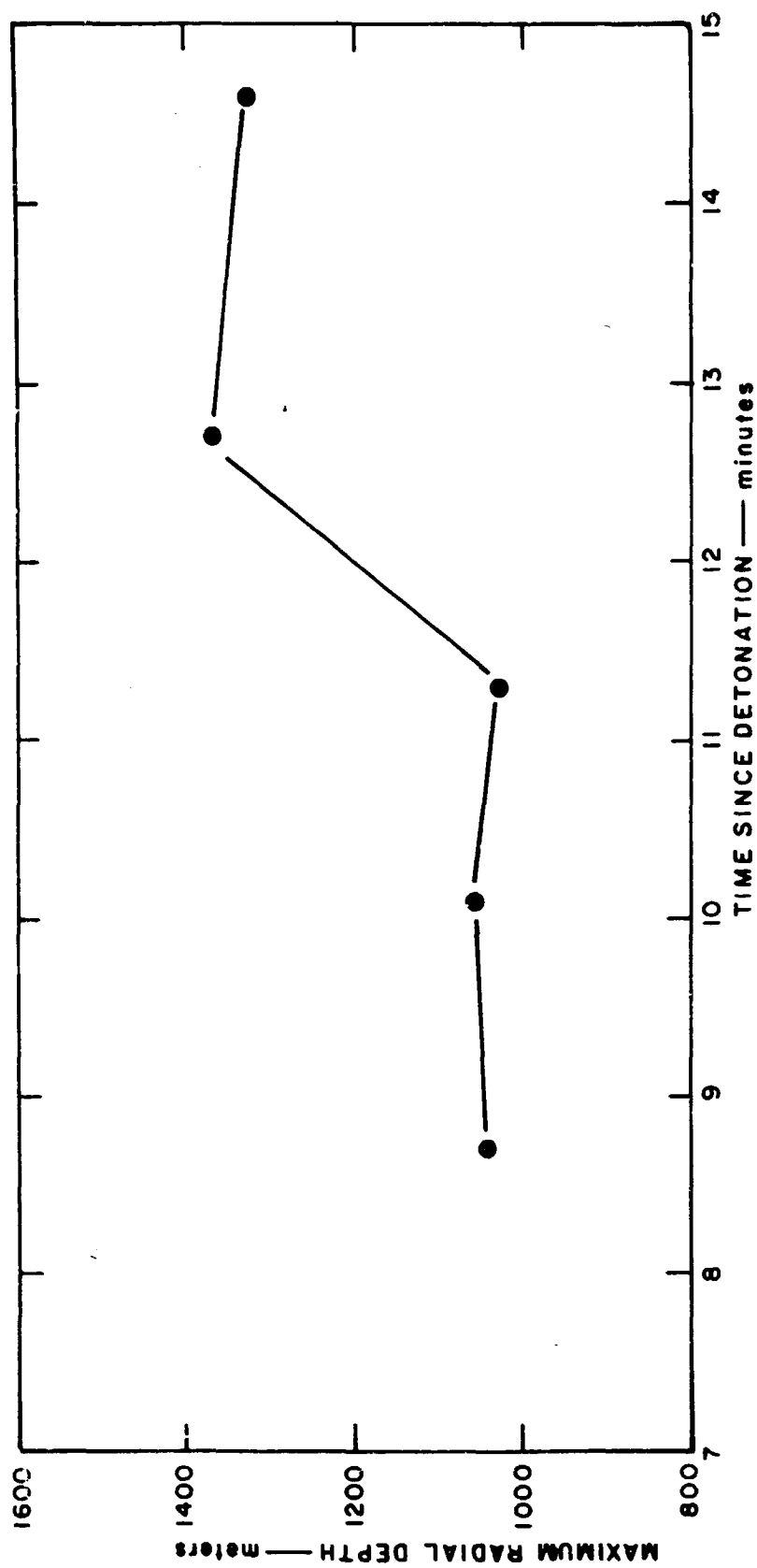


FIG. 21 RADIAL DEPTH OF SUB-VISIBLE CLOUD-ALFA

from some natural, sub-visible stratus-type cloud, their position and motion is quite compatible with their being due to the dust or moisture introduced by the explosion, and they could well be from the remains of the early, visible cap cloud. There was thermal inversion at approximately 656m and this could well have limited the vertical extent of the dust cloud or the cap cloud remains. It would equally, of course, have determined the height of stratus-type cloud, some of which were seen in the area later.

A rough indication of the events is given in plan view in Figure 22.

## 2. Further Analysis of the Data

Although uncertainties result from the limited sampling, some attempt to evaluate the backscattering coefficient of the clouds may be made. The definition of lidar backscattering cross section for a volume target is identical to that for microwave radar. The volume backscatter coefficient  $\beta'_{180}$  is defined as "the scattering cross section of an isotropic scatterer returning as much power to the lidar as the particles actually present."  $\beta'_{180}$  is expressed  $\text{km}^{-1}$ .

The volume backscattering coefficient of the target cloud is a component of the lidar range equation, which describes the behavior of the return signal in terms of equipment constants and the characteristics of the atmosphere and the target. The lidar equation is fundamental to most of the analysis techniques employed to extract useful information from the signal, and may be written as follows:

$$P_r = P_t \frac{A_r}{R^2} \frac{1}{4\pi} \frac{C\tau}{2} \beta'_{180}(R') T_o T_a e^{-2 \int_0^{R'} dR'} \quad (1)$$

where:  $P_r$  = Received power

$P_t$  = Transmitted power

— VISIBLE CLOUD HEIGHT: APPROX. 600 m.  
 - - - SUB-VISIBLE CLOUD HEIGHT: APPROX. 450 m.  
 - - - NEBULOUS RETURN HEIGHT: APPROX. 500 m.

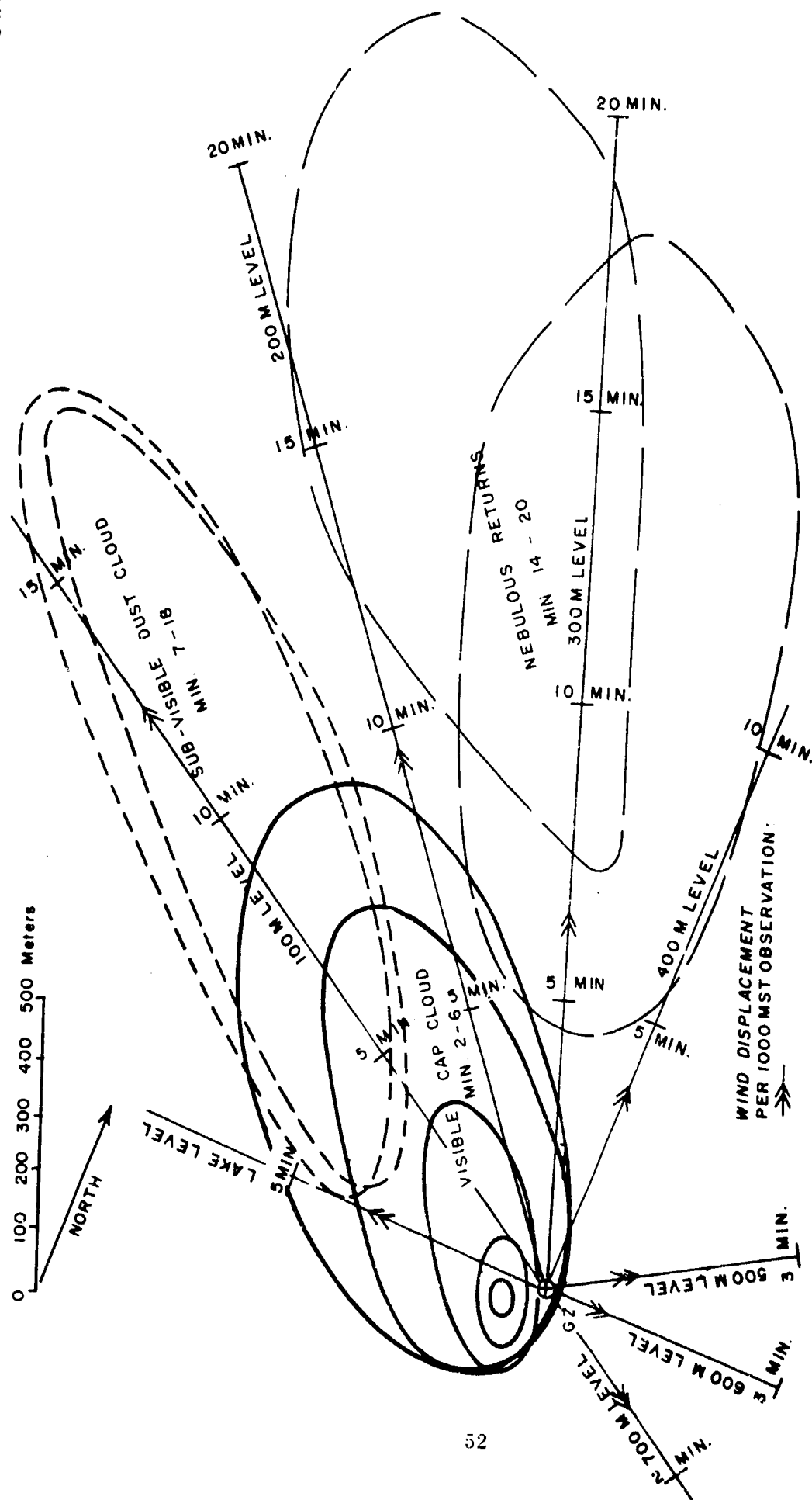


FIG. 22 PLAN VIEW - ROUGH INDICATION OF DISPERSAL OF THE THREE CLOUD PHASES—ALFA

$A_r$  = Effective area of receiver aperture

$C$  = Velocity of light

$\tau$  = Transmitter pulse length

$\beta'_{180}(R')$  = Volume backscattering coefficient at  $R'$

$T_o$  = Transmission efficiency of all optical componenets

$R$  = One-way distance to target

$R'$  = Penetration distance into target

$T_a$  = Atmospheric transmission factor accounting for total attenuation to and from the target

$\sigma$  = Extinction coefficient within target region

The backscatter-coefficient data of Figure 23 were obtained from the solution of Eq. (1) for  $\beta'_{180}(R')$ :

$$\beta'_{180}(R') \exp\left(-2 \int_0^{R'} \sigma dR'\right) = K_1 \frac{P_r R^2}{T_a} \quad (2)$$

Where  $K_1$  is a constant, dependent on the lidars parameters:

$$K_1 = \frac{8}{P_t A_R C T_o} \quad (3)$$

Equation (2) can be evaluated directly in terms of  $\beta'_{180}(R')$  for the special cases where the penetration distance into the cloud  $R'$  is small, or the value of extinction coefficient  $\sigma$  is small. This latter condition applies particularly when the target is too tenuous to be visible. The data of Figure 23, represent the value of  $\beta'_{180}(R')$  existing at the specific ranges where the lidar beam first enters the cloud.

Relative changes in the backscatter coefficient in the form of  $\log_{10} \beta'_{180}(R')$  vs. time are shown in Figure 23. Relative changes are shown, since the absolute value of received power  $P_r$  is difficult to measure accurately at the present time. However, relative changes in received power (and therefore  $\beta'_{180}$ ) may be accurately



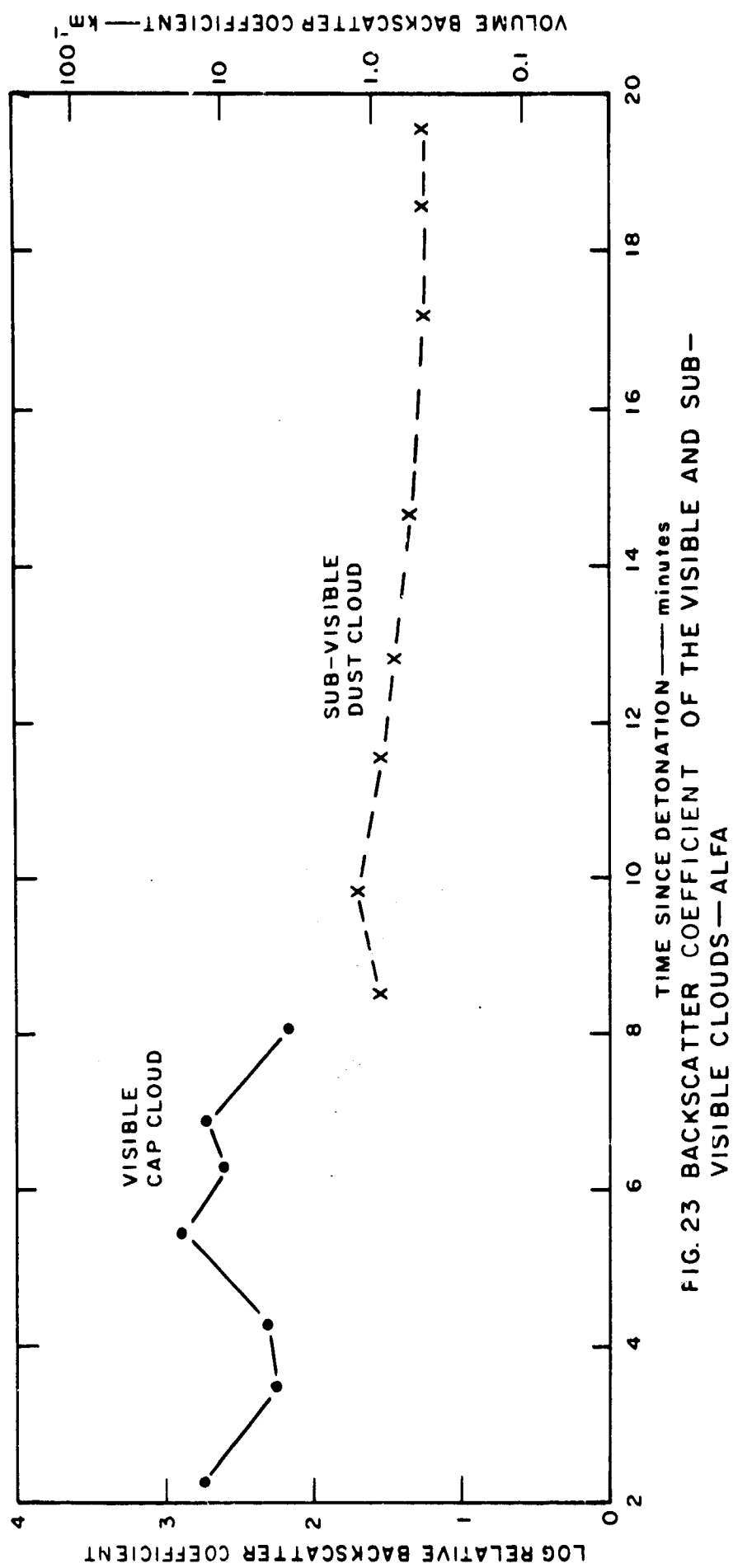


FIG. 23 BACKSCATTER COEFFICIENT OF THE VISIBLE AND SUB-VISIBLE CLOUDS—ALFA

measured.

Since the Pre-GONDOLA I test site was removed from any major sources of atmospheric pollution, Elterman's model of a clear atmosphere (Reference 4) may be used to estimate the value of atmospheric attenuation  $T_o$ , and its rate of increase with increasing range  $R$ . For a wavelength of  $1.06\mu$  and an altitude of 746 meters above sea level, this model gives an extinction coefficient of  $0.06 \text{ km}^{-1}$ , which corresponds to a two-way attenuation  $T_a$  of 0.52 dB per kilometer.

The maximum variation in range during the time interval of Figure 23 was approximately 0.9 km, resulting in a variation of  $T_a$  of 0.47 dB or 1.12:1.  $T_a$  was, therefore, assumed to be a constant for this analysis.

Absolute values of  $\beta'_{180}$  were obtained in the following way: the absolute sensitivity of the lidar is calculated for the magnitude of the clear atmosphere return at close range, assuming that the atmospheric reflectivity which produced this signal can be described in Elterman's model for a clear atmosphere. Once the lidar calibration factor is known, the value of  $\beta'_{180}$  corresponding to the return from the cloud at any range  $R$  can be readily calculated by correcting for the  $R^{-2}$  propagation law of the signal. The absolute values of  $\beta'_{180}$  are included on the right-hand ordinate of Figure 23, where the discontinuity between the visible cloud phase and the dust phase is apparent. In the visible cloud the effect of random sampling is apparent but in the more diffuse cloud phase, the observations are remarkably consistent.

The volume backscattering coefficient depends in a complex manner upon the number, size, and dielectric properties of the particles present. It is thus not possible at this time to derive precise information on the nature of an assemblage of particles from a single measurements of backscatter. Where the particles are of

of the same order of size or larger than the laser wavelength the volume backscatter coefficient varies in general terms with the summation of the cross sectional areas of the particles present. It is thus possible to deduce relative changes in the distribution of particulate material in the target cloud, but unless the particle size spectrum remains substantially constant, it is not possible to assess the changes in cloud density with precision.

The horizontal projections of the visible and sub-visible cloud are shown in Figures 24 through 36. These figures illustrate the cloud development and its motion over the ground. The method described in shot Charlie was used to obtain these projections; the details of the method will be discussed using the raw data of Figure 3 and the horizontal projections of Figure 26 as examples.

Referring to trace A of Figure 3, the slant ranges at which the lidar beam entered and left the cloud are indicated by the target return at 1.42 and 1.86 KM respectively. These slant ranges are converted to horizontal ranges by multiplying by the cosine of the lidar beam elevation angle ( $10^\circ$  in this case). For trace A, the ground ranges of 1.4 and 1.83 KM at an azimuth of  $334^\circ$  are plotted in Figure 26. This process is repeated for the remaining three traces of Figure 3, yielding azimuth and horizontal range data for a total of seven points which are also plotted on Figure 26. These points are connected by a smooth curve to form an outline of the cloud referenced to the lidar location and to ground zero.

Figure 37 illustrates the volume estimates of the visible and sub-visible cloud, which are obtained using the method described in shot Bravo. The apparent decrease in cloud volume during  $T_0 + 8$  minutes through  $T_0 + 10$  minutes and at  $T_0 + 17:30$  minutes may be attributed to inadequate sampling of the cloud, a limitation imposed by the firing rate of the lidar.

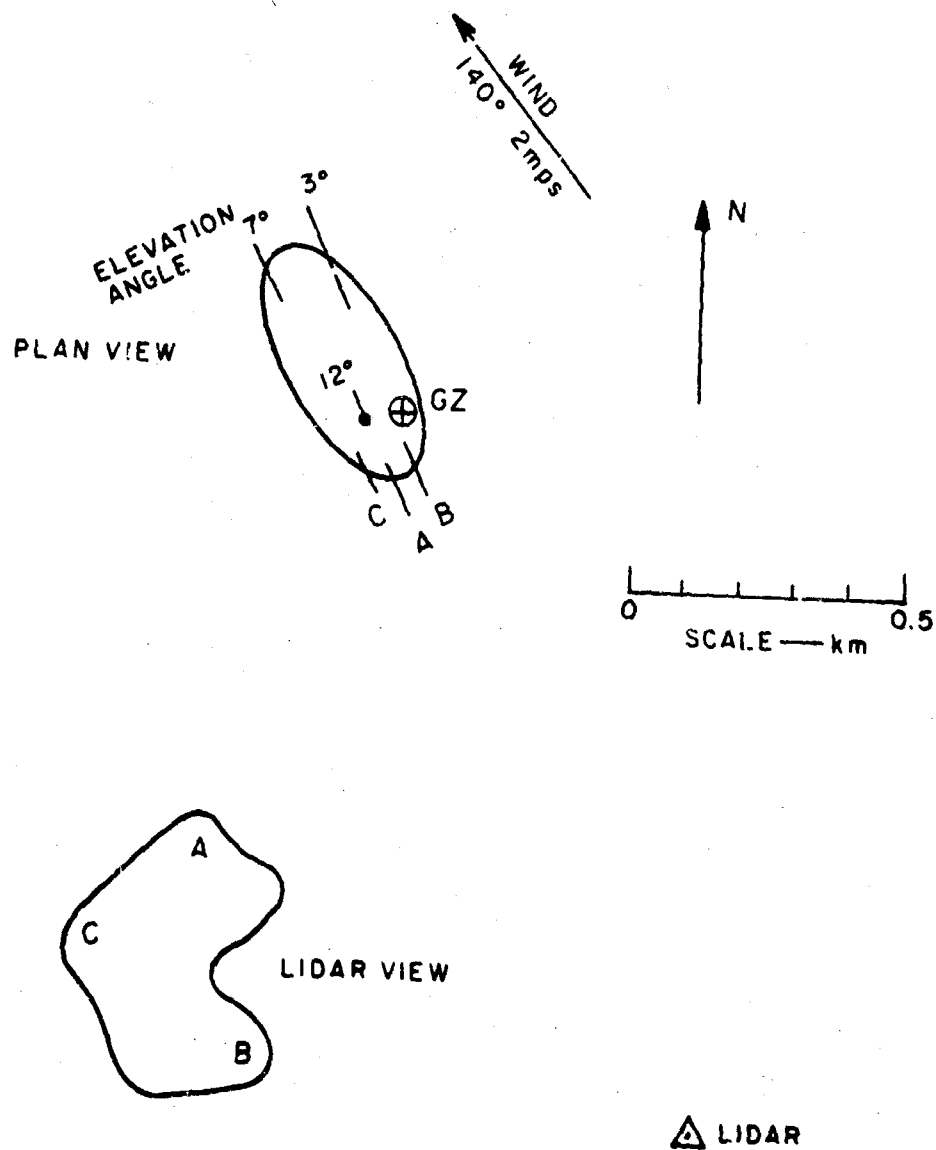


FIG. 24 HORIZONTAL PROJECTION OF THE VISIBLE CLOUD—  
ALFA, TIME: 1:42 to 2:18 min.

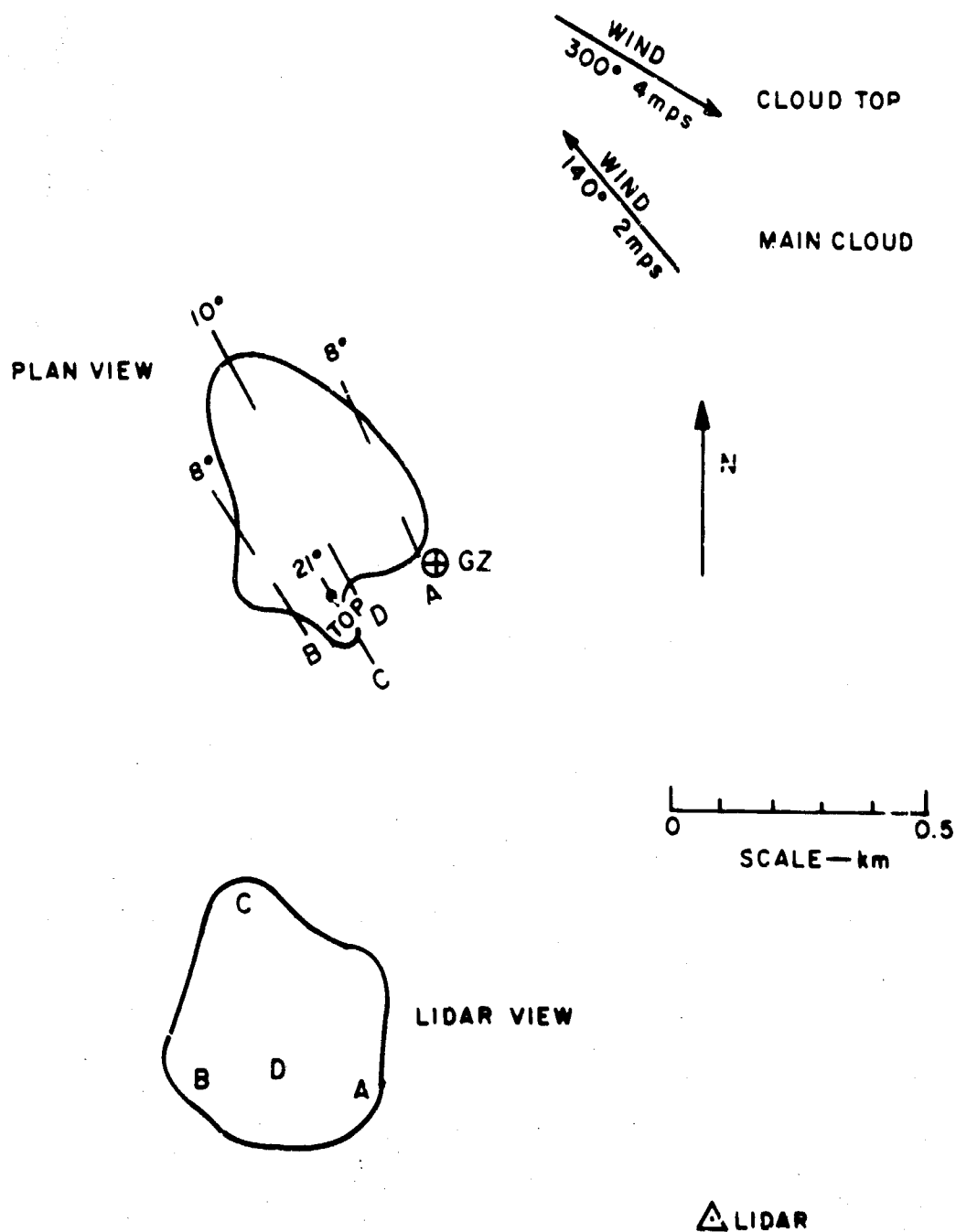


FIG. 25 HORIZONTAL PROJECTION OF THE VISIBLE CLOUD —  
ALFA, TIME: 2:49 to 3:27 min.

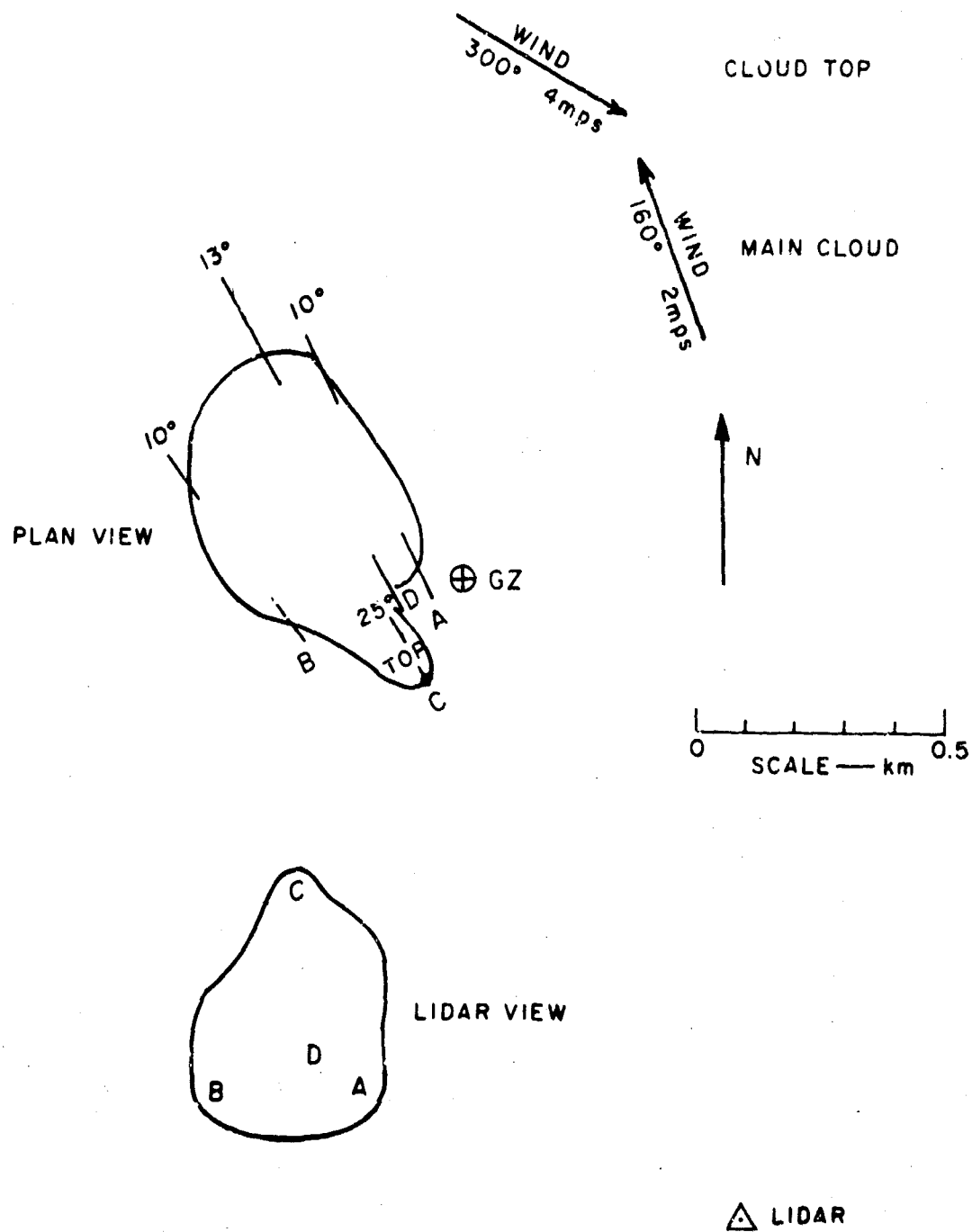


FIG. 26 HORIZONTAL PROJECTION OF THE VISIBLE CLOUD —  
ALFA, TIME: 3:47 to 4:17 min.

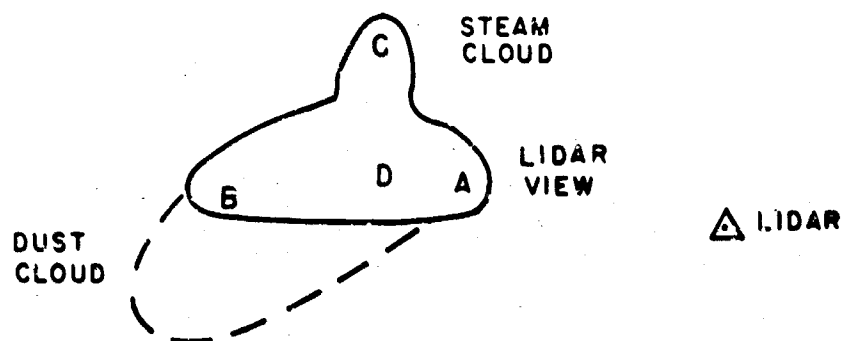
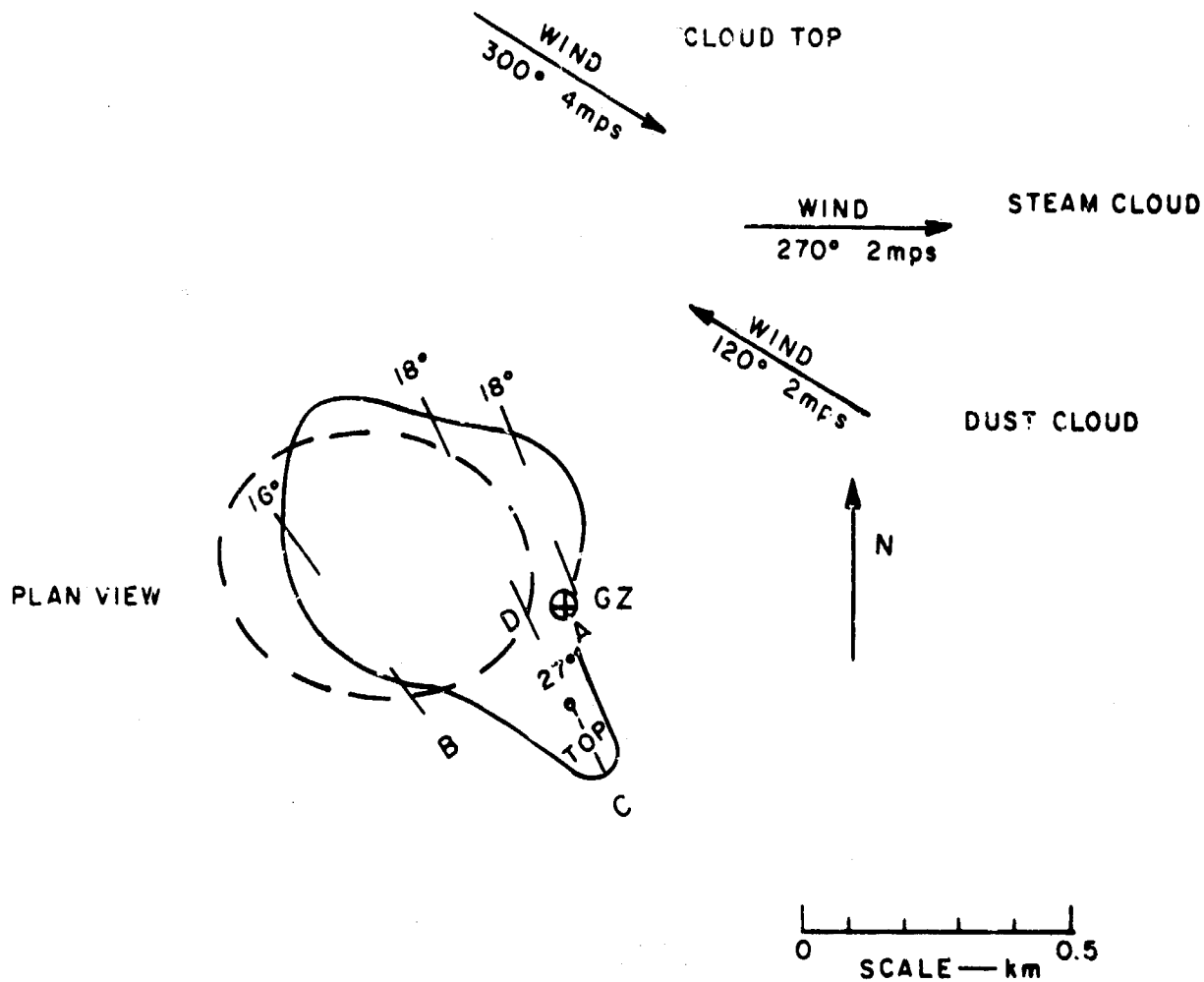


FIG. 27 HORIZONTAL PROJECTION OF THE VISIBLE CLOUD—  
ALFA, TIME: 4:44 to 5:22 min.

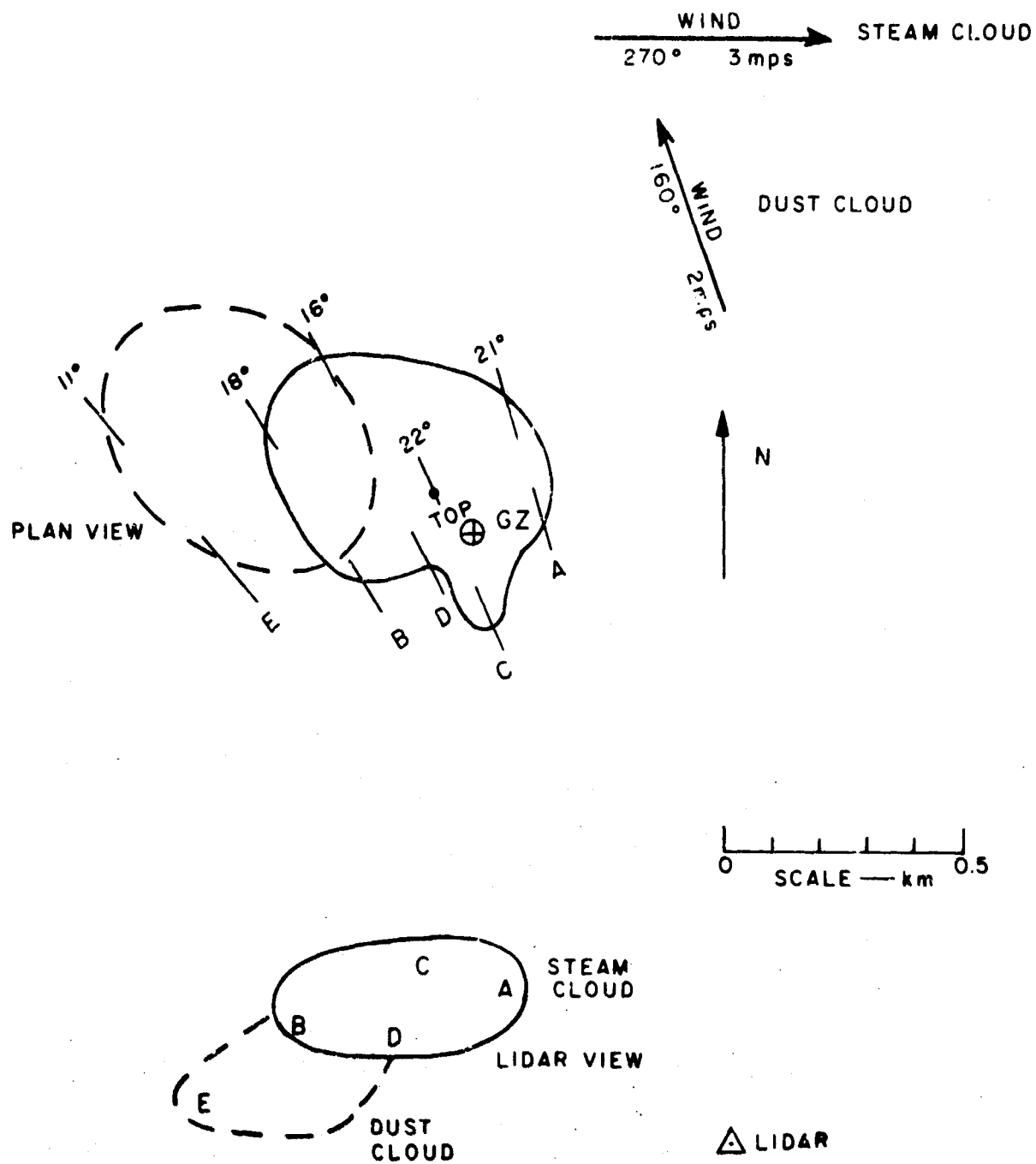


FIG. 28 HORIZONTAL PROJECTION OF THE VISIBLE CLOUD—  
ALFA, TIME: 5:43 to 6:32 min.



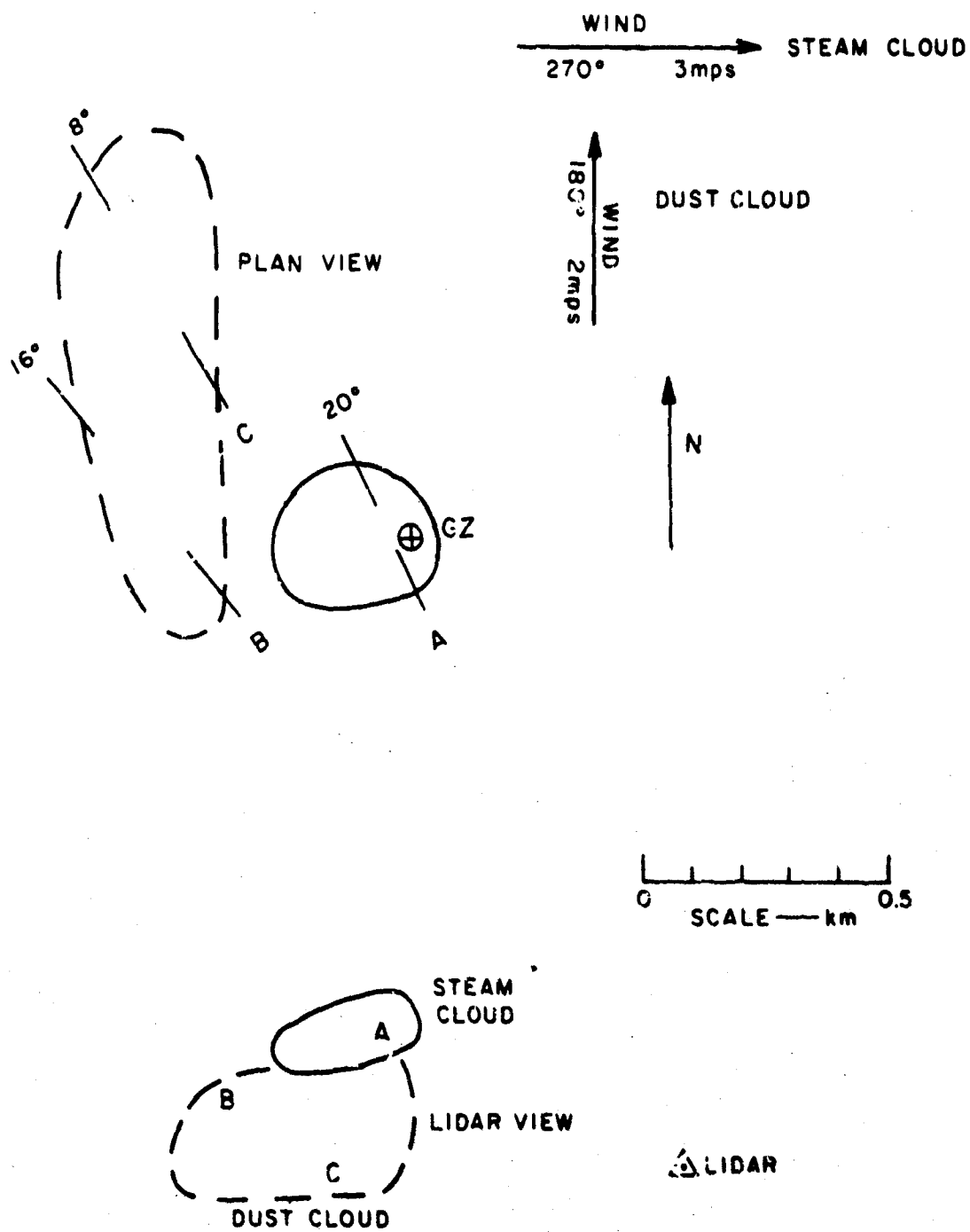


FIG. 29 HORIZONTAL PROJECTION OF THE VISIBLE CLOUD—  
ALFA, TIME: 6:59 to 7:41 min.

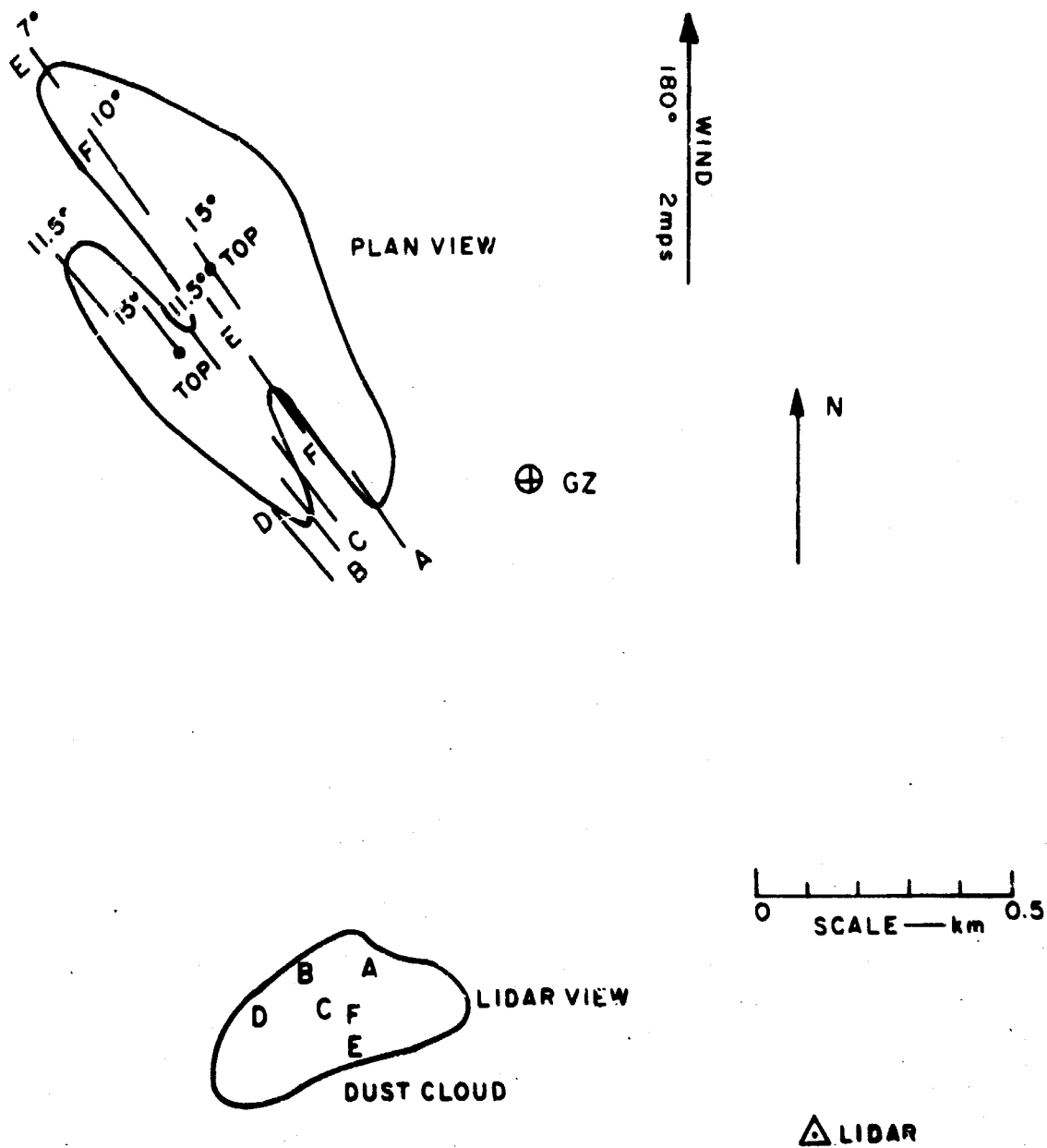


FIG. 30 HORIZONTAL PROJECTION OF THE VISIBLE CLOUD—  
ALFA, TIME: 3:20 to 9:17min.

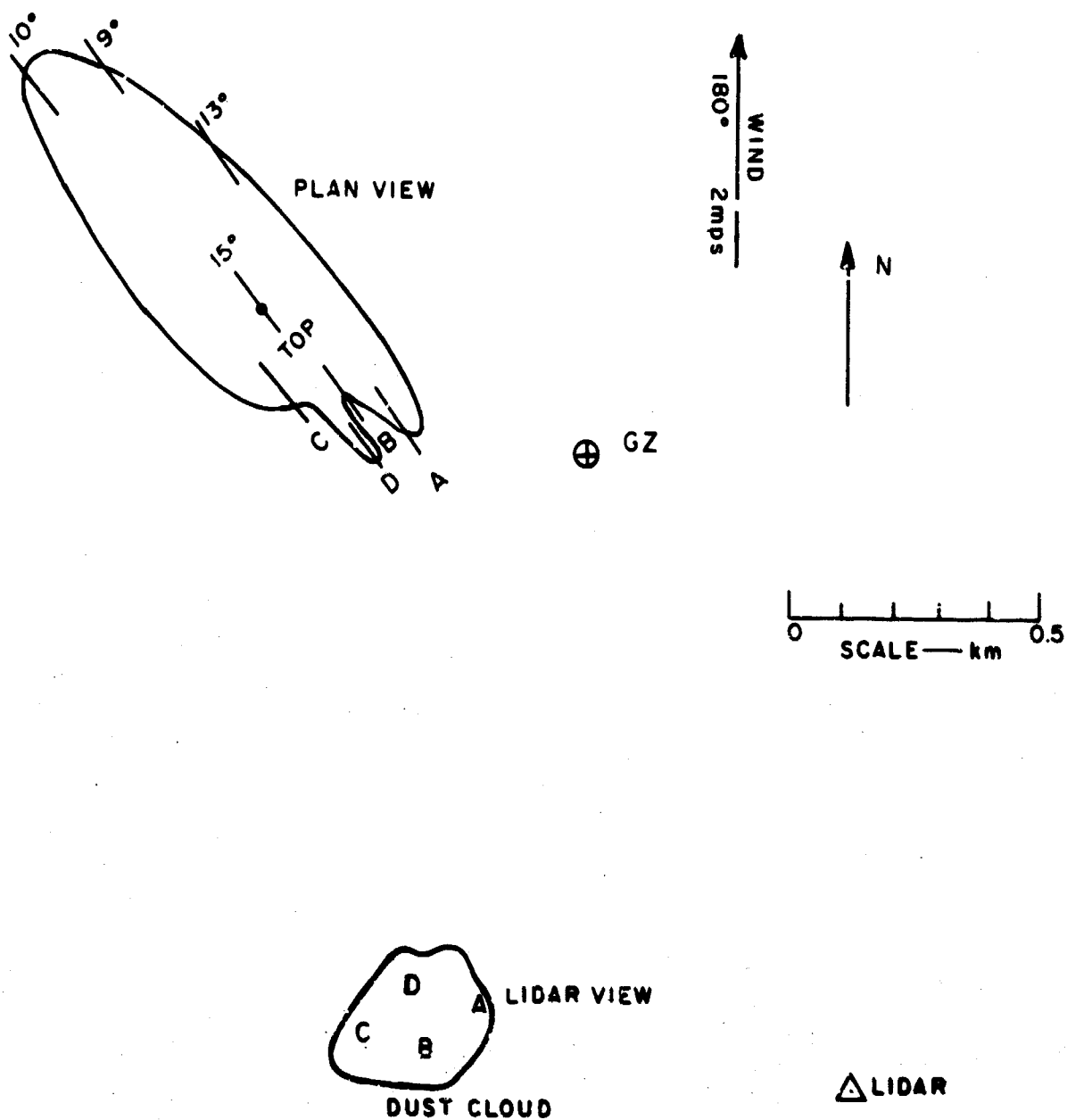


FIG. 31 HORIZONTAL PROJECTION OF THE VISIBLE CLOUD—  
ALFA, TIME: 9:46 to 10:27 min.

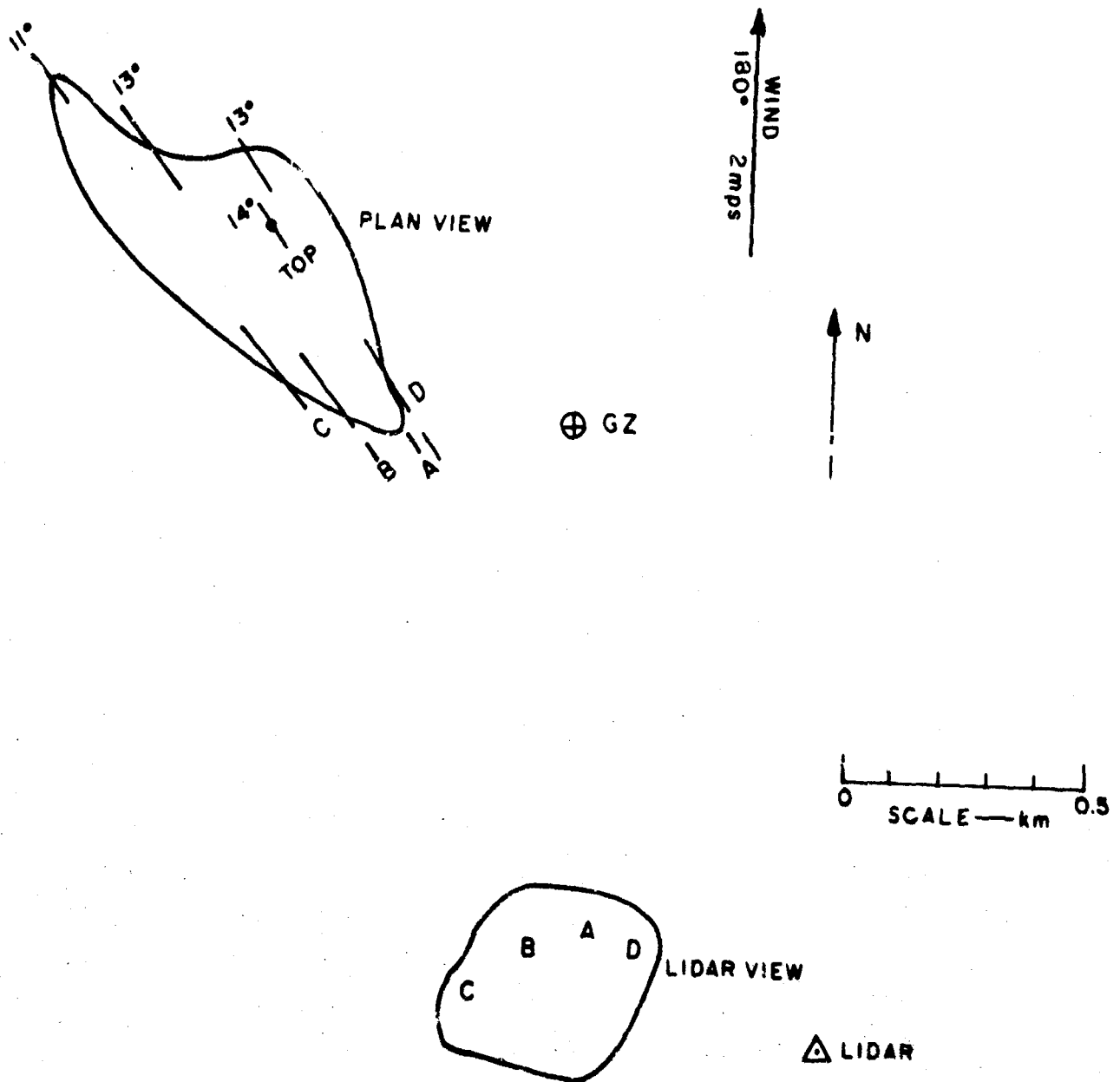


FIG. 32 HORIZONTAL PROJECTION OF THE VISIBLE CLOUD—  
ALFA, TIME: 10:54 to 11:41 min.

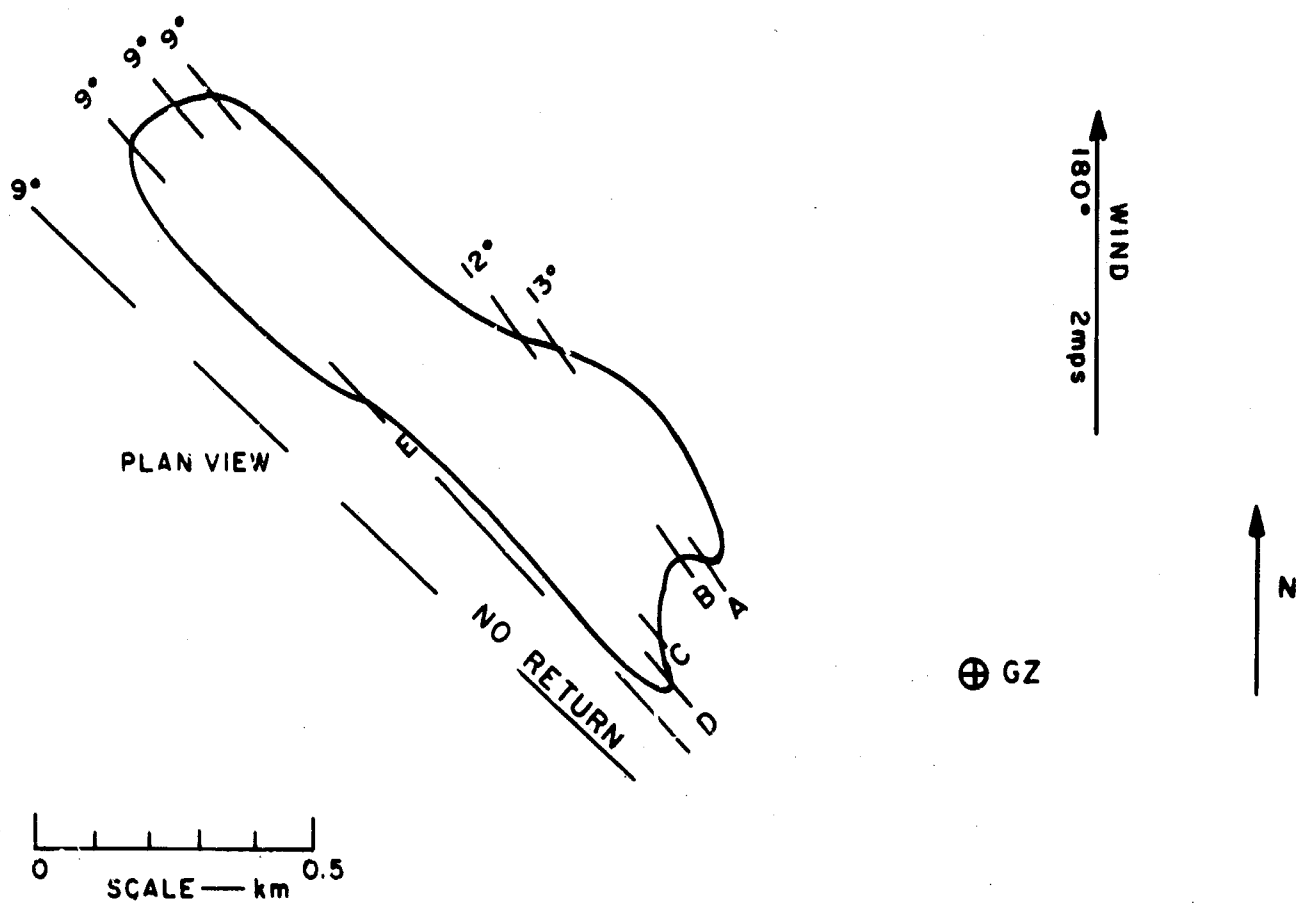


FIG. 33 HORIZONTAL PROJECTION OF THE VISIBLE CLOUD —  
ALFA, TIME: 12:10 to 13:31min.

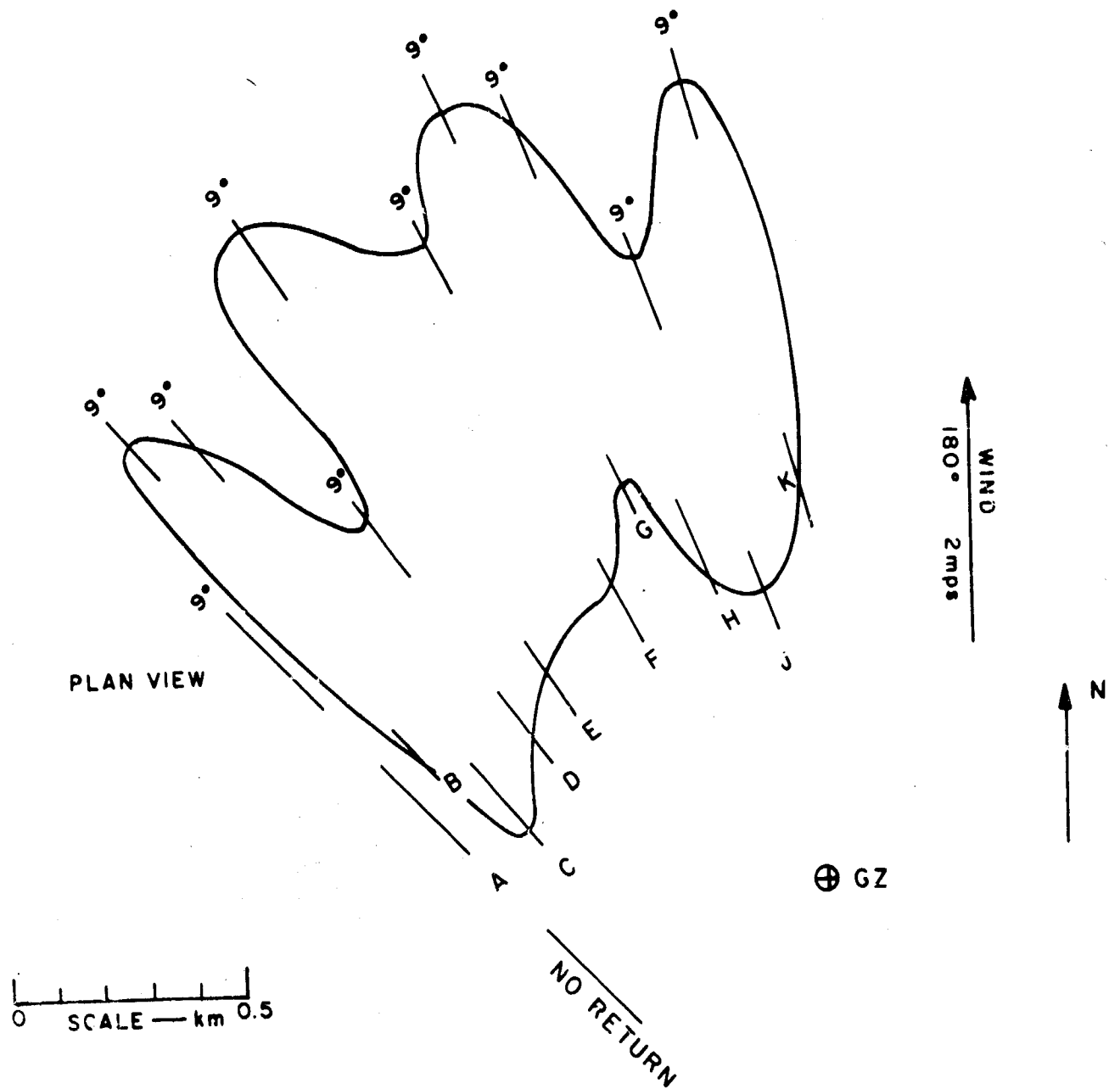


FIG. 34 HORIZONTAL PROJECTION OF THE VISIBLE CLOUD —  
ALFA, TIME: 14:07 to 16:20 min.

LIDAR  $\Delta$

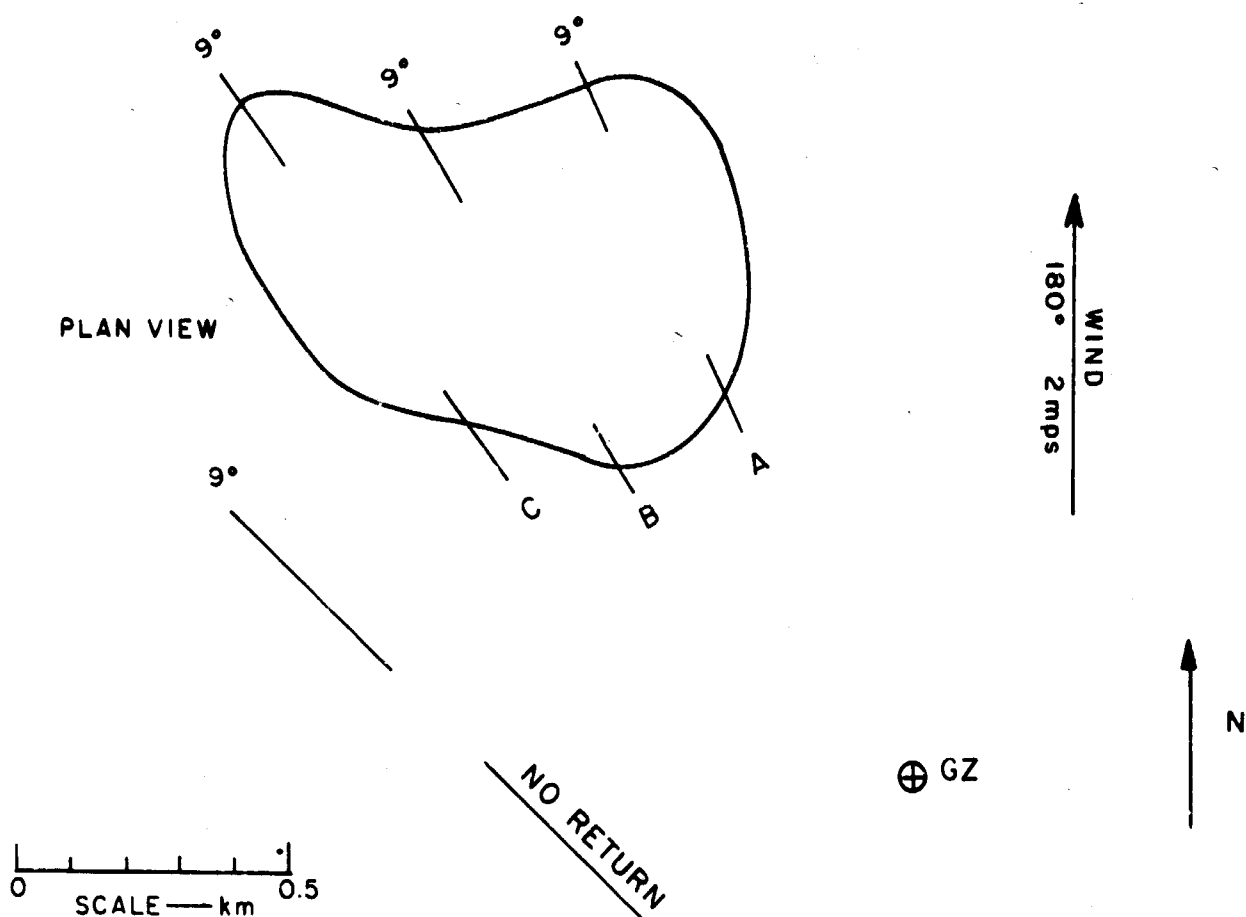


FIG. 35 HORIZONTAL PROJECTION OF THE VISIBLE CLOUD —  
ALFA, TIME: 17:01 to 18:00 min.

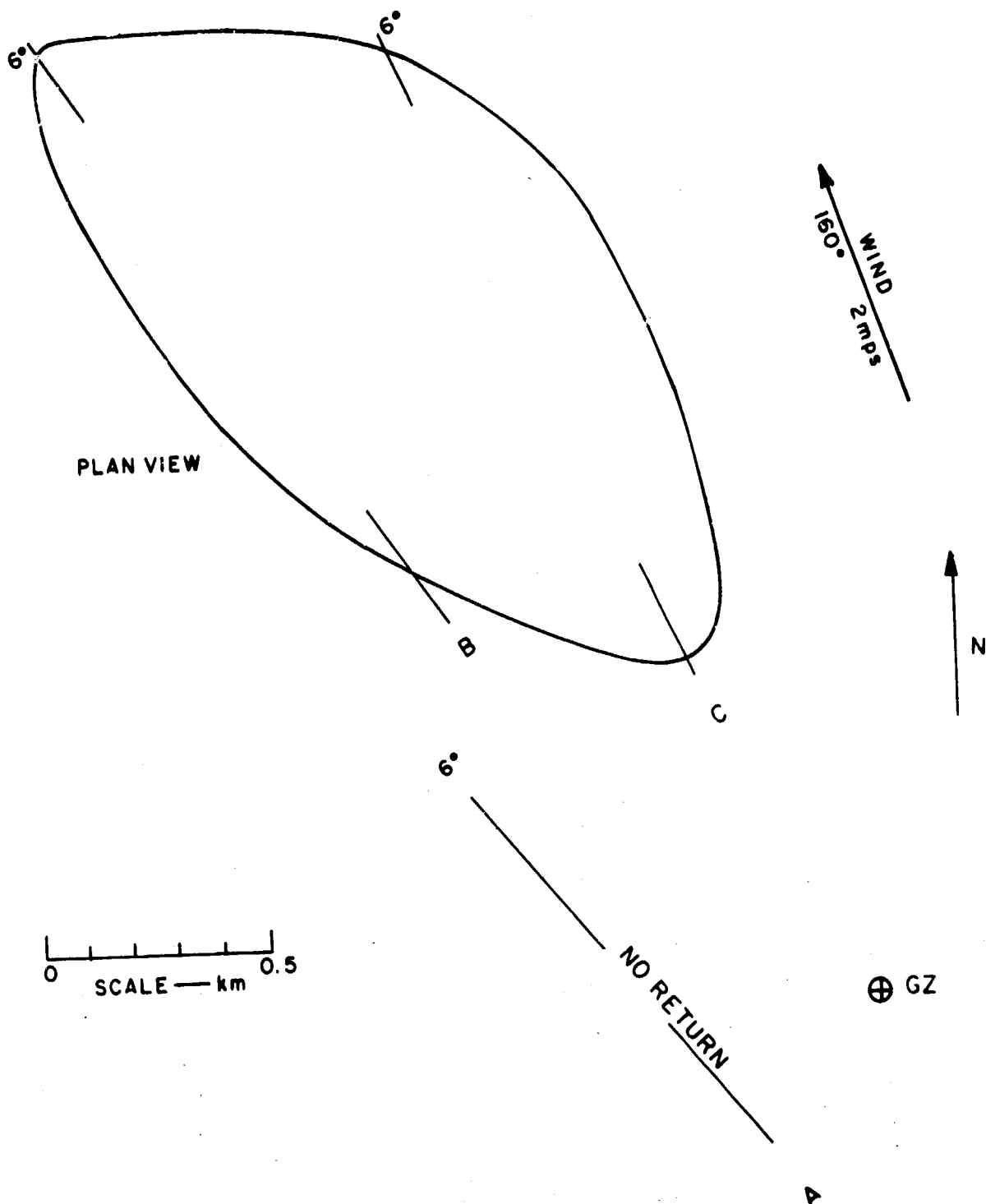


FIG.36 HORIZONTAL PROJECTION OF THE VISIBLE CLOUD—  
ALFA, TIME: 18:24 to 18:58min.



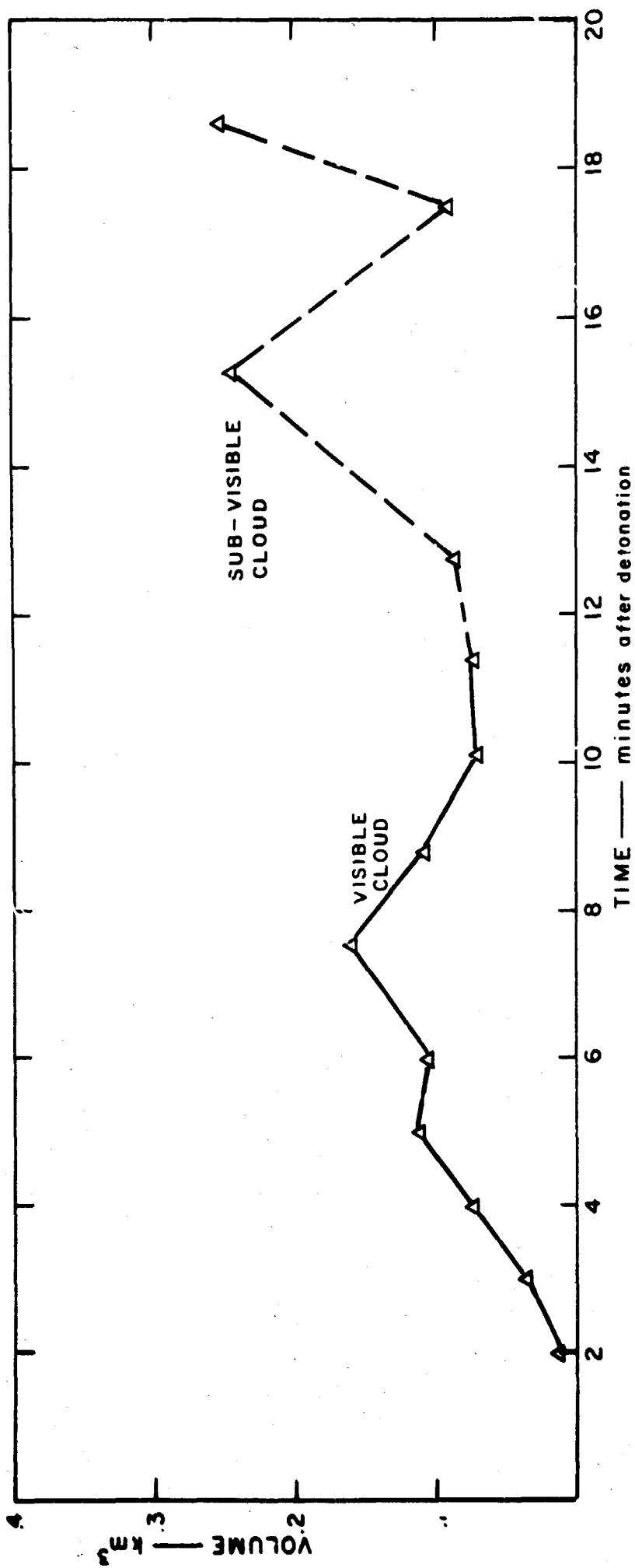


FIG. 37 VOLUME ESTIMATE OF VISIBLE AND SUB-VISIBLE CLOUD—ALFA,

#### D. Shot Delta, 4 November 1966

Shot Delta occurred on a cold, clear morning with some upper clouds, and temperatures in the low 20's. A fresh breeze from WNW was forecast to become more northerly and increase to 20 to 25 mph.

The SGZ was  $325^{\circ}$ (T) from the lidar and any wind from WNW to NNW would bring the cloud pretty well over the site. It was decided in this series of observations to attempt to establish shape and density variations in plan of the cloud at a given level--i.e., near the surface--with the hope of obtaining data on drop-out behavior and demonstrating the potential of high-PRF scanning systems in this role.

Accordingly, we established three plans. The first two covered the eventuality of the cloud passing overhead from the NW. The intention here was to obtain a vertical cross section. Plan I started with lidar at  $90^{\circ}$  elevation and Plan II with lidar at  $50^{\circ}$  elevation on azimuth  $030^{\circ}$ . In both plans we would start firing as soon as the Safety Officer gave permission. Then we would continue firing at maximum rate (intervals of approximately 50 sec) until the cloud had cleared the lidar site and no further echoes were seen. We would then depress to  $+0.5^{\circ}$  elevation and scan on a fixed program, first by  $2^{\circ}$  azimuth angle increments, and the  $1^{\circ}$ . In each plan the intention was to scan through the cloud and then scan back again.

The third plan (which was the one used with modification), was based on the cloud passing to the north of the lidar. Here the lidar would be aimed at  $030^{\circ}$  azimuth and  $0.5^{\circ}$  elevation, and fired in rapid sequence.

##### 1. Cloud Tracking

The explosion produced a rapidly towering cloud which had two main stems. The visible material was seen to trail up and out onto a cloud comparable to a small cumulus cloud, and this drifted to the ENE. Beneath this cloud a faint haziness indicated

the lower dust cloud, but this was very faint and soon became invisible. Although the lower portion of the cloud appeared very tenuous, Plan III was adopted and after an initial clear shot, echoes were received as the cloud moved across the lidar beam.

Judging by the motion and time of passage of the cloud, it appeared preferable to try another translation series on fixed azimuth rather than going immediately onto a scanning program. Accordingly, a new azimuth was selected at  $064^{\circ}$ . The forward motion of the cloud had been underestimated and after a false start, a second azimuth of  $085^{\circ}$  was selected. The first shot of the new series was a little late, but was undoubtedly quite near the leading edge of the cloud and the second series was run on this heading.

When the cloud had passed through and was clear, the prearranged scanning program at  $2^{\circ}$  and  $1^{\circ}$  azimuth increments was started. After the continued absence of returns indicated that the cloud was too weak to detect further, a tenuous cloud was seen at a higher level and was presumed to be the remains of the cap cloud. A few trial shots were made on this and at least one recorded a return. Systematic scanning in the vertical and horizontal failed to locate further echoes, however. The surface wind recorded at the CP was  $280^{\circ}$  15 mph (7.5 mps) at 10:00 MST. The average wind was fairly uniform, although gusty.

The experience gained in the Alfa and Delta observations strongly suggests that the main core of debris (dust) is fairly narrow and is very tenuous. In fact, it very soon becomes invisible as it disperses (and presumably loses matter by sedimentation). The upper cloud, which grows out of the main core, rolls out with possibly a vortex motion, and spreads out in classic (small) mushroom style. It then resembles a small cumulus cloud and, in fact, is very probably a "steam" cloud quite comparable to a cumulus. The "steam" cloud last 5 to 7 minutes, before it evaporates

in the dry air. Any interest in this aspect of the explosion is probably best served with conventional photographic methods, providing adequate contrast exists between the cloud and the background.

## 2 Data Analysis

The ground tracks of the visible and sub-visible clouds are shown in Figure 38. High-resolution contours of relative density variations existing near the base of the cloud at various times are shown in Figures 39, 40, and 41. The contours represent values of return-signal,  $P_r$ , \* expressed in dB referenced to the return produced by the clear atmosphere.

As discussed in Section IIC 4a above, these values do not correspond directly with reflectivity owing to the effects of attenuation. Again, the relationship between optical reflectivity and particulate matter content of the cloud is not precisely known. As a first approximation, however, the contours of relative signal intensity provide a very good basis for inferring the variations with respect to density.

---

\* Corrected for the  $R^{-2}$  propagation law, as in Eq. (2).

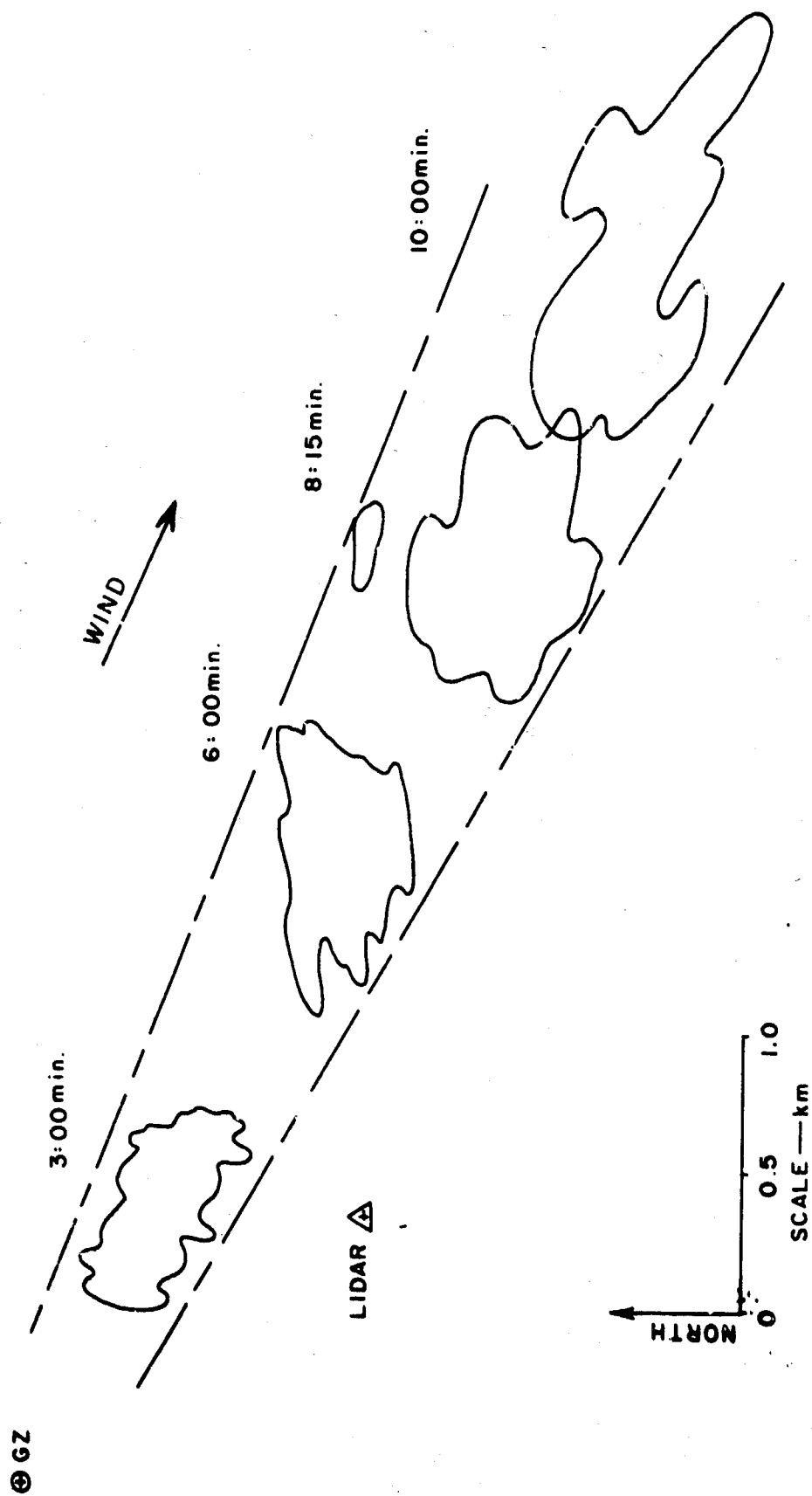


FIG. 38 DELTA EVENT—GROUND TRACK OF  
SUB-VISIBLE CLOUD

⊕ GZ

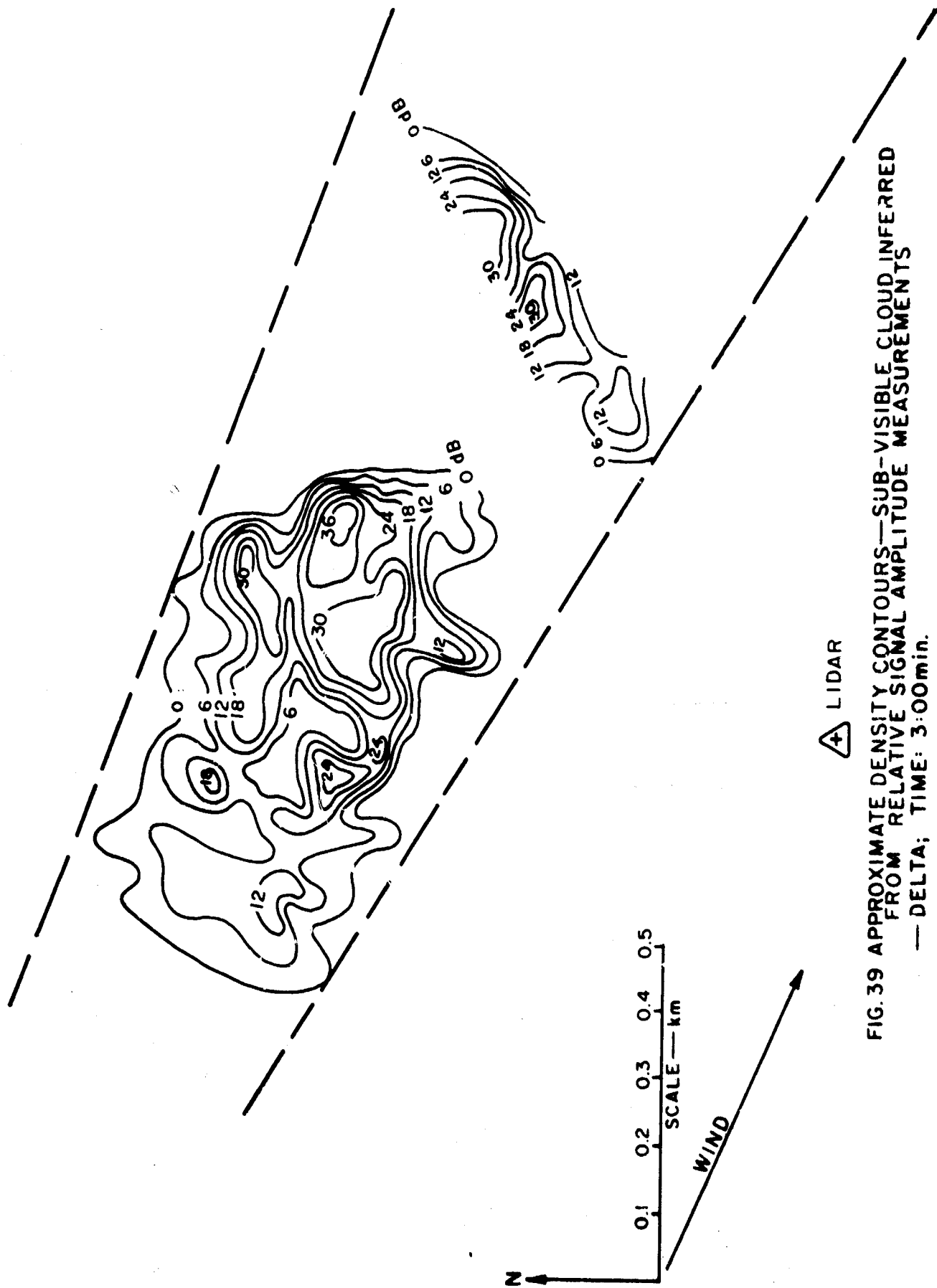


FIG. 39 APPROXIMATE DENSITY CONTOURS—SUB-VISIBLE CLOUD INFERRED  
FROM RELATIVE SIGNAL AMPLITUDE MEASUREMENTS  
— DELTA; TIME: 3:00min.

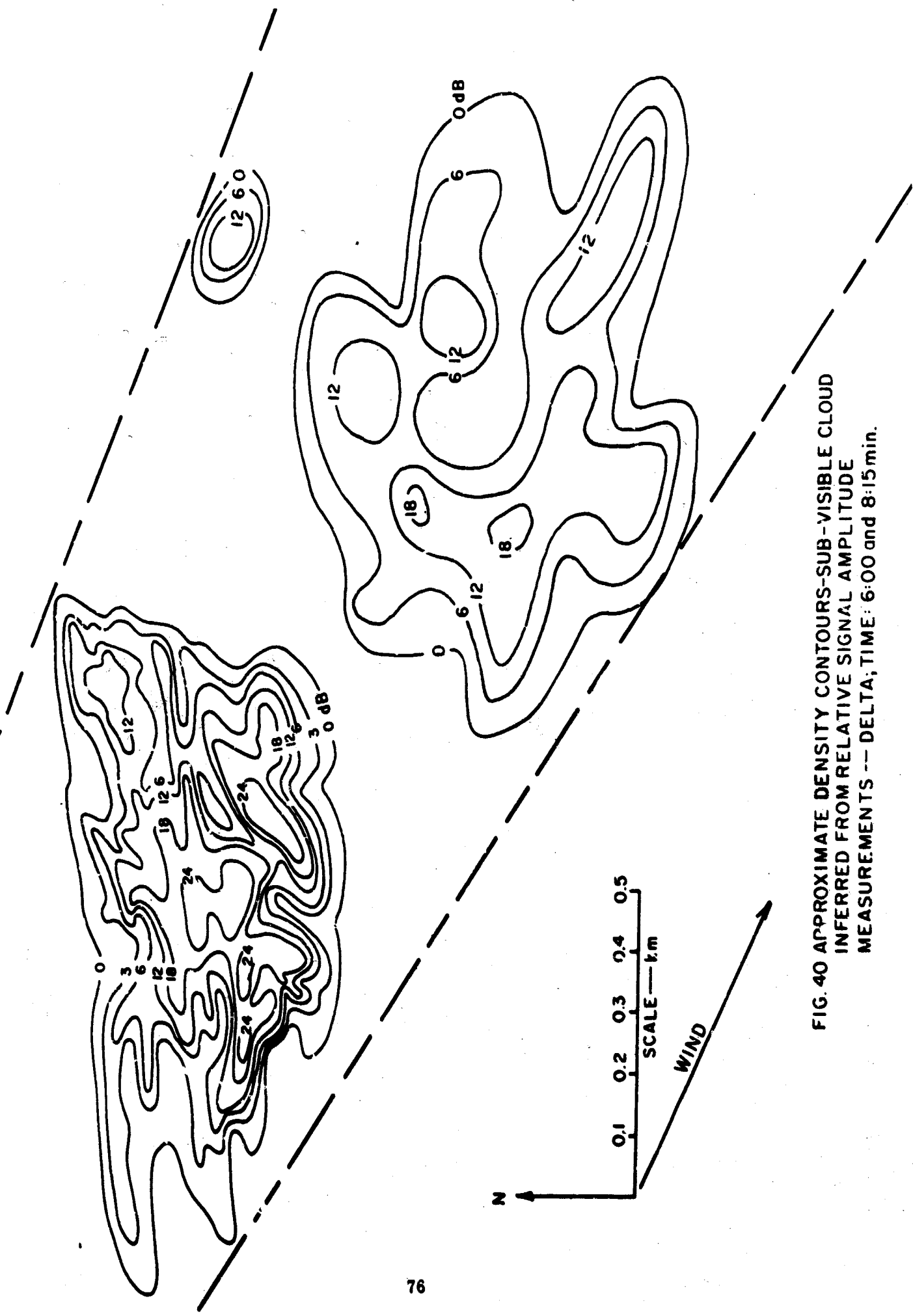


FIG. 40 APPROXIMATE DENSITY CONTOURS-SUB-VISIBLE CLOUD  
INFERRED FROM RELATIVE SIGNAL AMPLITUDE  
MEASUREMENTS -- DELTA; TIME: 6:00 and 8:15 min.

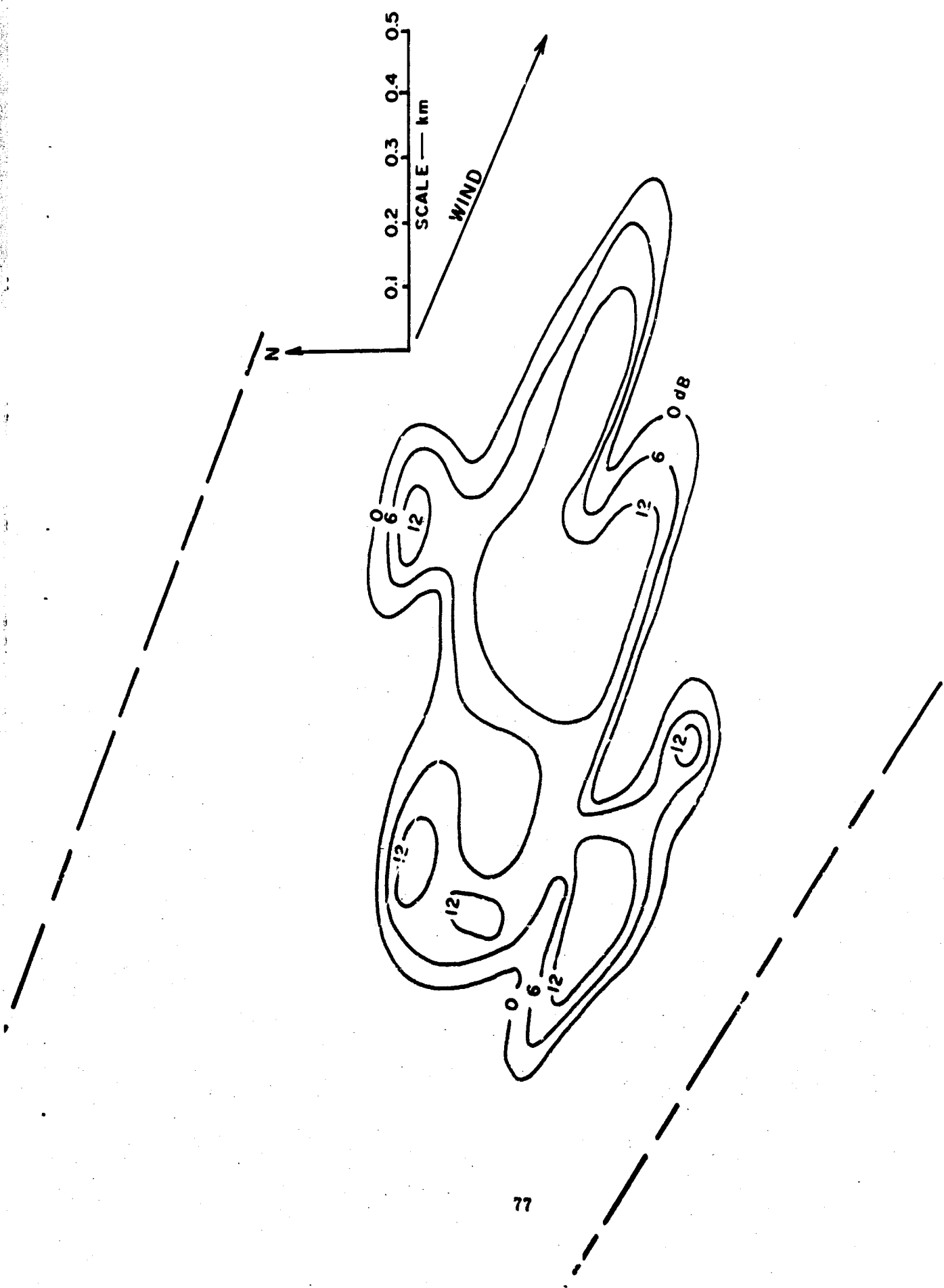


FIG. 41 APPROXIMATE DENSITY CONTOURS—SUB-VISIBLE CLOUD INFERRED FROM  
RELATIVE SIGNAL AMPLITUDE MEASUREMENTS—DELTA; TIME: 10: min.



#### REFERENCES

1. M. G. H. Lidga, "The Laser in Meteorology," Discovery (July 1965)
2. R. T. M. Collis, "Lidar: A New Atmospheric Probe," Quart. J. Roy. Meteorol. Soc. Vol. 92, p. 392 (April 1966)
3. C. A. Northend, R. C. Honey, and W. R. Evans, "Laser Radar (Lidar) for Meteorological Observation," Review of Scientific Instruments, Vol. 37, No. 4, pp. 393-400 (April 1966)
4. L. Elterman, "Atmospheric Attenuation Model, 1964, in the Ultra-violet, Visible and Infrared Regions for Altitudes up to 50 km," AFCRL 64-740, Air Force Cambridge Research Laboratories, USAF (1964).

# APPENDIX

## PRE-GONDOLA TECHNICAL REPORTS

<u>Title of Report</u>	<u>Agency</u>	<u>Author and/or Technical Program Officer</u>	<u>Report Number</u>
<u>Pre-GONDOLA -</u>			
Seismic Site Calibration	NCG	M. K. Kurtz B. B. Redpath	PNE 1100
Site-Selection Investigations	NCG/Omaha	H. A. Jack W. W. Dudley	PNE 1101
<u>Pre-GONDOLA I -</u>			
Technical Director's Summary Report	NCG	M. K. Kurtz <u>et al</u>	PNE 1102
Geologic and Engineering Properties Investigations	NCG/Omaha	P. R. Fisher <u>et al</u>	PNE 1103
Close-in Ground Motion, Earth Stress, and Pore Pressure Measurements	WES	J. D. Day <u>et al</u>	PNE 1104
Intermediate Range Ground Motion	LRL	D. V. Power	PNE 1105
Structures Instrumentation	WES	R. F. Ballard	PNE 1106
Crater Studies:			
Crater Measurements	NCG	R. W. Harlan	PNE 1107 Part I
Surface Motion Studies	NCG	W. G. Christopher	PNE 1107 Part II
Cloud Development Studies	NCG/LRL	W. C. Day R. F. Rohrer	PNE 1108
Close-in Displacement Studies	AFWL	C. J. Lemont	PNE 1109
Lidar Observations of Pre-GONDOLA I Clouds	SRI	J. W. Oblanas R. T. H. Collis	PNE 1110
Pre-Shot Geophysical Measurements	LRL-N	R. T. Stearns J. T. Rambo	PNE 1111